Moragas, M., Vergés, J., Nalpas, T., Saura, E., Martín-Martín, J.D., Messager, Gré., Hunt, D.W., The impact of syn- and post-extension prograding sedimentation on the development of salt-related rift basins and their inversion: Clues from analogue modelling, Marine and Petroleum Geology (2017), doi: 10.1016/j.marpetgeo.2017.10.001.

The impact of syn- and post-extension prograding sedimentation on the development of salt-related rift basins and their inversion: Clues from analogue modelling

Mar Moragas[a], Jaume Vergés[a], Thierry Nalpas[b], Eduard Saura[a], Juan Diego Martín-Martín[a, c], Grégoire Messager[d], David William Hunt[d]

[a] Group of Dynamics of the Lithosphere (GDL), Institute of Earth Sciences Jaume Almera, ICTJA-CSIC, Lluís Solé i Sabarís s/n, 08028 Barcelona, Spain

[b] Géosciences Rennes, UMR CNRS 6118, Université de Rennes 1, OSUR, Campus de Beaulieu, 263 Avenue Leclerc, 35042 Rennes Cedex, France

[c] Departament de Mineralogia, Petrologia i Geologia Aplicada. Universitat de Barcelona, Martí i Franquès s/n, 08028 Barcelona, Spain

[d] Statoil Research Centre, Bergen, Norway

Keywords: Analogue modelling, inverted salt-related rift basins, prograding sedimentation, Central High Atlas

Highlights (3 to 5 with 85 characters including spaces)

- Tectono-sedimentary interplay in salt-related rift basins is studied in seven models
- Different sedimentary patterns influenced the growth of diapirs at a basin scale
- Reactive–active, roller-like, passive, and extrusive diapirs developed in models

- Inversion caused flank steepening, close-up, and final welding of existing diapirs

Abstract

Various studies have demonstrated the intrinsic interrelationship between tectonics and sedimentation in salt-related rift basins during extension as well as during their inversion by compression. Here, we present seven brittle–ductile analogue models to show that the longitudinal or transverse progradation of sediment filling an elongate extensional basin has a substantial impact on the growth of diapirs and their lateral geometrical variations. We use five extensional models to reveal how these prograding systems triggered diapir growth variations, from proximal to distal areas, relative to the sedimentary source. In the models, continuous passive diapir walls developed, after a short period of reactive–active diapiric activity, during syn-extensional homogeneous deposition. In contrast, non-rectilinear diapir walls grew during longitudinal prograding sedimentation. Both longitudinal and transverse post-extensional progradation triggered well-developed passive diapirs in the proximal domains, whereas incipient reactive–active diapirs, incipient roller-like diapirs, or poorly developed diapirs were generated in the distal domains, depending on the modelled sedimentary pattern. Two models included final phases of 6% and 10% shortening associated with basin inversion by compression, respectively, to discriminate compressional from purely extensional geometries. With the applied shortening, the outward flanks of existing diapir walls steepened their dips from 8°–17° to 30°–50°. Likewise, 6% of shortening narrowed the diapir walls by 32%–72%, with their fully closing (salt welds) with 10% of shortening. We compare our results with the distribution of salt walls and minibasins of the Central

High Atlas diapiric basin in Morocco, which was infilled with a longitudinally prograding mixed siliciclastic and carbonatic depositional sequence during the Early–Middle Jurassic with a minimum thicknesses of 2.5–4.0 km.

1. Introduction

Analogue modelling has become an essential tool for studying the mechanisms involved in tectonic processes such as lateral compression, extension, and strike-slip tectonics (e.g., Dooley and Schreurs, 2012; Graveleau et al., 2012; Koyi, 1997; McClay, 1996). Analogue modelling has been applied to the study of salt tectonics to obtain a better understanding of the mechanisms that trigger the onset of diapirs and the evolution of diapiric structures and minibasins (Brun and Fort, 2004; Nalpas and Brun, 1993; Schultz-Ela and Jackson, 1996; Vendeville and Jackson, 1992; Weijermars et al., 1993). The geometries generated by these models have been compared with the large number of high-resolution seismic lines imaging salt-related provinces in various parts of the world, such as along the Atlantic passive margins (Fort et al., 2004; Krézsek et al., 2007), the Gulf of Mexico (Dooley and Hudec, 2017; Ge et al., 1997a; Rowan and Vendeville, 2006), and the North Sea (Dooley et al., 2003, 2005; Ge et al., 1997b).

Analogue modelling has allowed the relationship between extension and the development of coeval salt diapirs to be defined (e.g., Dooley et al., 2005; Koyi et al., 1993; Schultz-Ela and Jackson, 1996; Vendeville and Jackson, 1992, amongst others). Post-salt sedimentary layers deposited over an active basement graben filled with salt may stretch laterally by a combination of extension and bending. Continuous regional extension and the drag folding of post-salt strata may trigger reactive–active diapirism followed by a phase of passive diapirism whose evolution depends on the thickness of the source layer, the thickness of the overburden, and the rate of sedimentation (Jackson and Vendeville, 1994; Vendeville and Jackson, 1992). In cases where the salt layer was deposited over a faulted basement, the extension above and below the salt can be partially coupled depending on the thickness of the salt layer and the velocity of extension (Dooley et al., 2003, 2005; Nalpas and Brun, 1993; Vendeville et al., 1995; Vendeville and Jackson, 1992), and therefore the basement geometry influences the extensional structures developed in the post-salt layers. Dooley et al. (2005) designed analogue models in extension with a complex faulted basement, some of them later inverted, generating extensional grabens in the overburden that influenced the location of the diapirs. In most previous models of salt-related basins, the sedimentation during extension and coeval diapiric evolution was homogeneous, with uniform sedimentation along the entire model device, that it may not always be realistic. Consequently, in the present study we designed diverse depositional patterns within a salt-related rift basin to evaluate the potential impact of such patterns on the underlying salt migration and on the evolution of the salt structures.

Together with the study of extensional regimes, modelling studies have been used to examine the impact of the progradation of a sedimentary system over a ductile layer. It has been shown that the progradation of a sedimentary wedge mobilises a ductile substrate into a variety of geometries, with the proximal part of the prograding system being characterised by the formation of half-grabens and the growth of diapirs, whereas the distal part undergoes the development of fold-and-thrust belts in which well-developed diapirs are also observed (Koyi, 1996; McClay et al., 1998, 2003; Talbot, 1992; Vendeville, 2005). Previously published analogue models have shown that the geometry and distribution of diapirs increase in complexity with: (i) the progradation of a sedimentary lobe, where the radial shape of the prograding system generates a complex network of polygonal or circular depocentres separated by salt ridges (Gaullier and Vendeville, 2005; Loncke et al., 2010); (ii) the topography of the rigid basement beneath the ductile layer and the consequent variation in the thickness of the mobile silicone representing salt (Dooley et al., 2017; Ge et al., 1997a); and (iii) the confluence of two sedimentary wedges (Guerra and Underhill, 2012).

Our experiments are based on natural examples from a case study in the Central High Atlas (Morocco), a Triassic–Jurassic rift basin inverted during the Alpine Orogeny. In the Atlas system, large basement faults limit thick Permo-Triassic half-grabens filled by siliciclastic deposits, volcanic lavas from the Central Atlantic Magmatic Province and Triassic–Jurassic evaporitic deposits (Courel et al., 2003; Oujidi et al., 2000). Permo-Triassic structures were buried under thick Early and Middle Jurassic successions displaying spectacular halokinetic deformation structures related to ENE–WSW-trending diapiric structures (e.g., Saura et al., 2014; Martín-Martín et al., 2017). Thus, our study aimed to characterise i) the extensional structures below and above the Upper Triassic salt-bearing deposits, ii) the effects of longitudinal versus transverse sedimentation on the growth of salt walls and on the development of minibasins in the Central High Atlas salt-related rift basin, and iii) the impact of the Alpine inversion on diapiric structures of the Central High Atlas. To attain these objectives, we present three sets of analogue models with an initial configuration of a single symmetric graben and designed them in accordance with the three main tectonic events defined in the study region (rift, post-rift, and inversion). Different depositional configurations are considered in each model during and after the rifting phase.

2. Geological setting

The Central High Atlas range is a doubly verging fold-and-thrust belt that formed as a result of the inversion of a Triassic–Jurassic rift basin during the Alpine Orogeny (Arboleya et al., 2004; Beauchamp et al., 1999; Frizon de Lamotte et al., 2000; Laville et al., 1977; Mattauer et al., 1977; Piqué et al., 2000; Teixell et al., 2003; Tesón and Teixell, 2008). In the central part of the range, the most common materials cropping out are Lower to Middle Jurassic deposits that form broad synclines or tabular plateaux separated by NE–SW-trending anticlines or thrust faults (Fig. 1). The cores of the anticlines, or ridges, are composed of Triassic evaporite-bearing shales and sandstones, commonly intruded by Middle to Late Jurassic gabbros (Frizon de Lamotte et al., 2008; Hailwood and Mitchell, 1971; Jossen and Couvreur, 1990; Laville and Harmand, 1982). The origin of these ridges has classically been attributed to various processes, including Jurassic compressional folding associated with reverse faults (Studer and Du Dresnay, 1980), Jurassic transpression along NE-trending sinistral strike-slip faults associated with en échelon opening (Laville and Piqué, 1992), the emplacement of Jurassic intrusions (Laville and Harmand, 1982; Schaer and Persoz, 1976), or the uplift of the borders of tilted blocks during extensional faulting (Jenny et al., 1981; Poisson et al., 1998). Only a few studies of local structures have proposed a diapiric origin for these ridges; for example, the Tazoult ridge (Bouchouata, 1994; Bouchouata et al., 1995), the Ikerzi ridge (Ettaki et al., 2007), the Tassent ridge (Michard et al., 2011), and the Toumliline diapir (Ayarza et al., 2005; Teixell et al., 2003). However, recent studies have interpreted the Central High Atlas as a complex diapiric basin in which more than ten elongated minibasins bounded by salt walls have been identified (Saura et al., 2014). Observed halokinetic stratal relationships in sediments flanking the ridges, as well as facies distribution analysis conducted in various minibasins throughout the Central High Atlas, show that diapir activity occurred from the Pliensbachian (and possibly earlier) to the Callovian (and possibly later) (Bouchouata, 1994; Bouchouata et al., 1995; Ettaki et al., 2007; Grélaud et al., 2014; Ibouh et al., 2011; Joussiaume, 2016; Malaval, 2016; Martín-Martín et al., 2017; Teixell et al., 2017; Vergés et al., 2017).

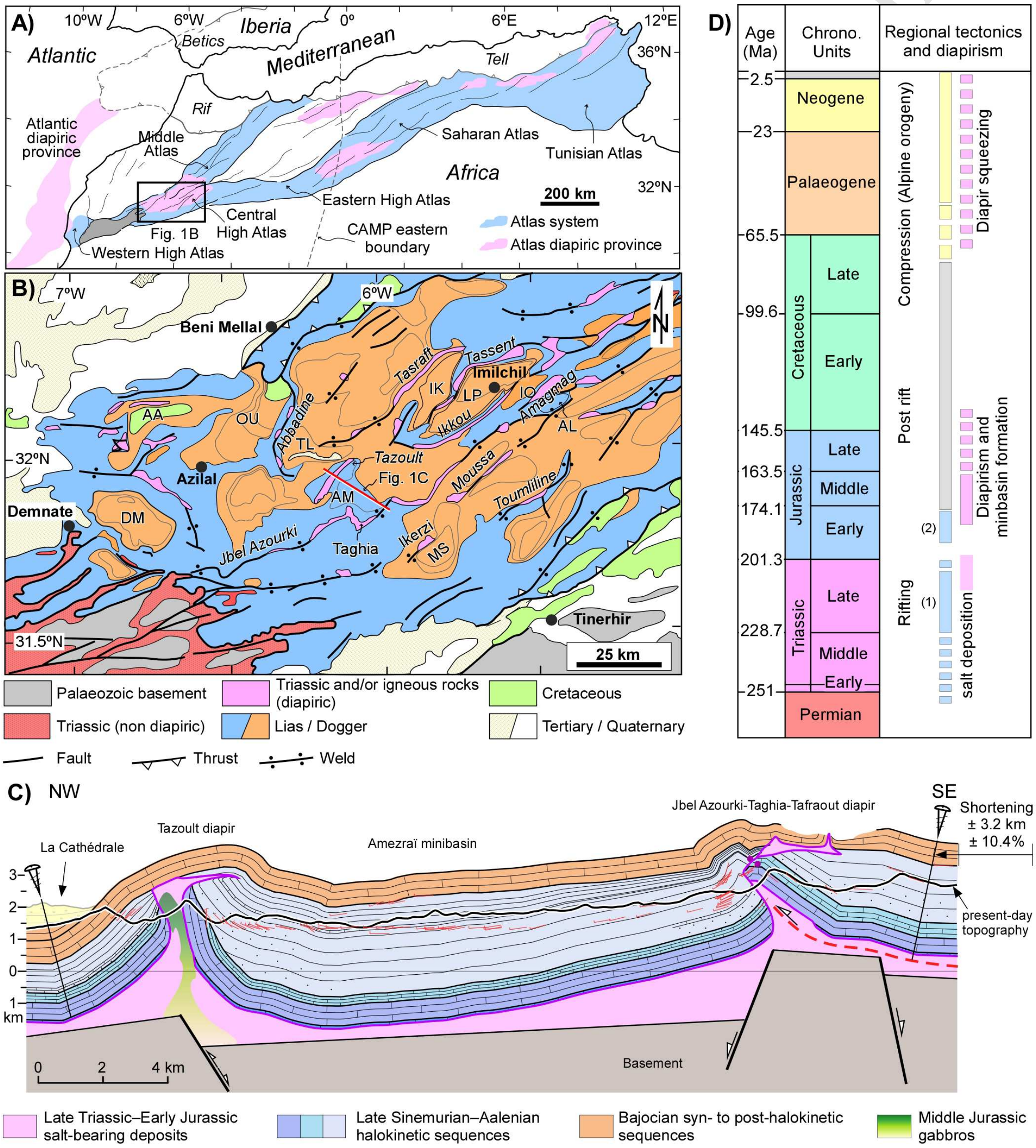

Fig. 1 (A) Synthetic map of NW Africa showing the locations of diapiric areas (pink). Central Atlantic Magmatic Province labelled as CAMP (B) Geological map of the Central High Atlas showing the locations of diapiric ridges and associated minibasins labelled as follows: Aït Attab (AA); Almghou (AL); Amezraï (AM); Demnate (DM); Ikassene (IK); Ikkou (IO); Lake Plateau (LP); Ouaouizaght (OU); and Tiloughite (TL). (Modified from Martín-Martín et al., 2016 and Saura et al., 2014). (C) Balanced cross-section across the Amezraï minibasin from Martín-Martín et al., 2016. (D) Chart showing the age of geodynamic processes occurring in the Central High Atlas (modified from Vergés et al., 2017). Two rifting phases have been differentiated: (1) late Permian to Late Triassic and (2) late Sinemurian to late Pliensbachian.

After the Variscan orogeny, the Central High Atlas underwent two consecutive rifting phases (Fig. 1D). The first rifting phase spanned from the late Permian to the Late Triassic, but with greater activity during the Middle–Late Triassic (Frizon de Lamotte et al., 2009; Laville et al., 2004). This extensional event caused the development of half-grabens bounded by high-angle normal faults with a dominant dip-slip movement filled. These grabens were filled with Upper Triassic continental red beds up to 2 km thick and were associated with the local development of thick evaporitic successions (Baudon et al., 2009; Courel et al., 2003; Domènech et al., 2015; Oujidi et al., 2000). After a short period of tectonic quiescence from the Hettangian to the early Sinemurian (from 201.3 to 195 Ma), renewed extension occurred from the late Sinemurian to the Pliensbachian (from 195 to 182.7 Ma); this was followed by a long post-rift period extending through the onset of the basin inversion during the Alpine Orogeny, when shortening occurred at rates of about 0.3 mm/yr on average (Ellouz et al., 2003; Frizon de Lamotte et al., 2009; Moragas et al., 2016; Tesón and Teixell, 2008). Palaeoreconstructions for the Jurassic (Fig. 2) show that the Central High Atlas basin was open towards the east, with the main direction of prograding sedimentation being oriented along the basin from WSW to ENE with the leading edge perpendicular to the basin margins (Milhi et al., 2002; Pierre et al., 2010; Piqué et al., 2000; Souhel et al., 2000). Our physical models were designed to simulate the processes occurring in the central part of the Atlas diapiric basin (Fig. 2), where the Tazoult and Jbel Azourki-Tafraout structures bounding the Amezraï basin are located (Fig. 1). Although the major depositional direction in the Central High Atlas during the Early and Middle Jurassic was longitudinal, we also present a model with transverse deposition to analyse the influence of both of these sedimentation patterns on diapir evolution and basin configuration.

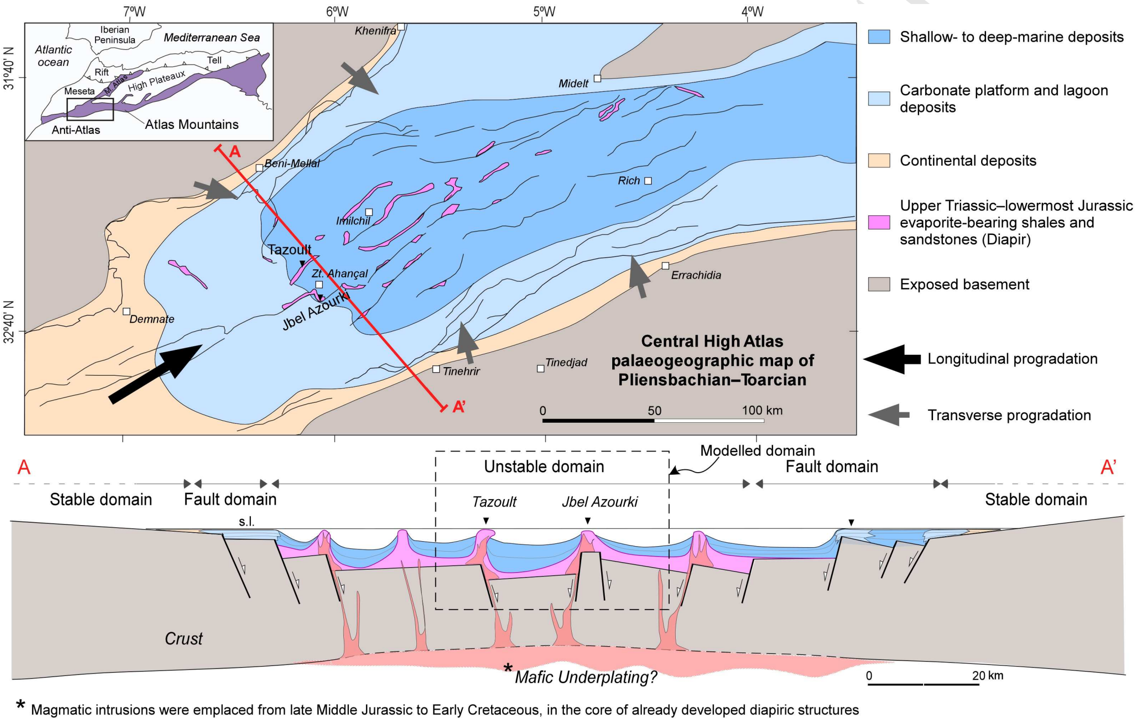

Fig. 2 Palaeogeographic map of the Central High Atlas basin for the late Pliensbachian to Toarcian period (modified from Moragas et al., 2016). Arrows indicate the direction of sediment input and progradation of the sedimentary systems in the basin. Cross-section A–A' shows an inferred configuration of the Atlas rift system tectono-sedimentary domains during the Early Jurassic and the interplay between normal faulting, diapir growth, and igneous intrusions above potential mafic underplating at the base of the crust.

3. Modelling procedure and experimental design

We used the classical techniques applied in brittle–ductile analogue modelling experiments, with the use of sand and silicone (Faugère and Brun, 1984), developed by the Experimental Tectonics Laboratory of Géosciences Rennes (Université de Rennes 1, France). The scaling of models to nature was chosen from published laws (Davy and Cobbold, 1991; Hubbert, 1937; Ramberg, 1981; Weijermars et al., 1993). A length of 1 cm in the models represents 0.8 km in nature (1.2×10^{-5}), and a time of 1 hour represents 3 Myr (1.14×10^{-10}) (Fig. 3).

To simulate the brittle behaviour of sedimentary rocks with Mohr–Coulomb properties, dry Fontainebleau quartz sand (produced by SIBELCO, France) was used in the experiments, with a mean grain size of approximately 250 μm, an internal friction angle of 30°–35° (Krantz, 1991), and a density (ρ) of approximately 1500 kg/m^3 (Fig. 3). Sand layers of different colours but the same mechanical behaviour were used as passive markers to emphasise the resultant structures. Transparent silicone was used to simulate salt, as it has been shown to be a suitable analogue material for this rock type (Weijerman et al., 1993). The mean viscosity of the silicone was ~3×10^4 Pa·s at 20 °C, and its mean density was ~1000 kg/m^3 (silicone polymer SGM 36, manufactured by Dow Corning, USA).

The modelling device used in this study was designed to simulate the Central High Atlas, where salt deposits were accumulated in the Triassic rift basin (Figs 1 and 2). The initial model set-up, comparable with but simpler than those presented in Dooley et al. (2005), simulated the inherited rift geometry from the Triassic rifting, with three rigid blocks representing the basement geometry and a central graben infilled with a thicker silicone layer and bounded by two faults dipping 60° (Fig. 3). The footwall blocks were fixed to mobile walls, whereas the central hangingwall block was not fixed, allowing it to subside during extension. A constant velocity of 0.5 cm/h was applied to each mobile wall by a screw jack during both lateral extension and compression, resulting in a total deformation velocity of 1 cm/h (equivalent to 0.2 mm/yr in nature). The ductile silicone layer representing the syn-rift salt was covered by a thin pre-extension brittle layer of 1 cm of sand (Fig. 3), which represented a sedimentary succession deposited during a short period of tectonic quiescence prior to renewed extension (Fig. 1D).

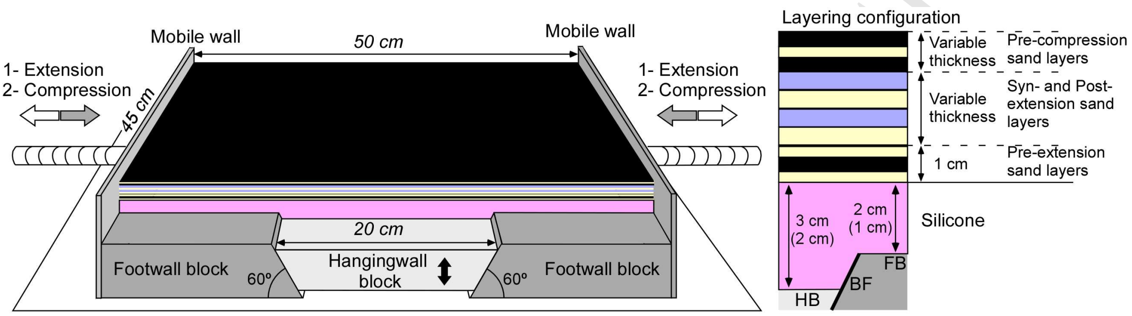

Scaling parameters

	Length (L)	Gravity (g)	Dry quartz sand density (ρ)	Décollement layer density (ρ)	Décollement layer viscosity (η)	Time
Nature	800 m	9.81 m/s^2	2.6 g/cm^3	salt 2.2 g/cm^3	salt 1 x 10^{19} Pa ·s	3 x 10^6 yr
Model	1 cm	9.81 m/s^2	1.5 g/cm^3	silicone 1.0 g/cm^3	silicone 3 x 10^4 Pa ·s	1 h
Model/nature ratio	1.2 x 10^{-5}	1	0.57	0.45	3 x 10^{-15}	1.14 x 10^{-10}

Fig. 3 The experimental modelling apparatus, consisting of a single central graben bounded by two fault planes dipping inwards at 60°. The column on the right-hand side of the figure shows the configuration of the different layers in the model (HB: Hangingwall block, FB: Footwall block, BF: Basement fault). The silicone thickness values in parentheses correspond to the thicknesses used in Model A1. The table details the scaling parameters.

The evolution of salt-influenced rift basins was analysed by running three sets of models (Fig. 4) representing the three main post-Triassic tectonic phases of the Central High Atlas (Fig. 1D): Early Jurassic rifting (extension), post-rift (tectonic quiescence), and Alpine inversion (compression). The influence of different amounts of sedimentation on diapir geometry was determined by varying the sedimentation thicknesses and patterns during the extension and post-extension phases (Fig. 4). Model A1 represented the evolution of the system during extension (2 h, equivalent to 6 x 10^6 yr, with a total extension of 2 cm, equivalent to 1.6 km) without the influence of sedimentation. Model set B (four models) represented the evolution of the system during extension, with sedimentation rates being equal to the accommodation rate (that combines the subsidence of the central block plus silicone expulsion), followed by a post-extension phase (3 h, equivalent to 9 x 10^6 yr) with a sedimentation rate equal to or lower than the rate of diapir growth. Model set C (two models) represented homogeneous sedimentation during the extension and post-extension phases and included a final compression phase with shortening (perpendicular to the rifting tectonic trends) of 3 cm (6%) and 5 cm (10 %), respectively (Fig. 4). The aim of Models C1 and C2 (Fig. 4) was to simulate a compressional event after diapirism in order to analyse the resulting geometries and basin deformation. The extension and compression phases of Models C1 and C2 were run using the same deformation velocity (1 cm/h), the same time lengths for the extension and post-extension phases (2 and 3 h, respectively), and the same sedimentation pattern (i.e., homogeneous during the extension and post-extension phases). This was designed to make to ensure that any differences between the resulting geometries were caused by the compression phase (Fig. 4).

Photographs of the surface of each model were taken every 6 minutes, corresponding to 0.1 cm of deformation during the extension and compression phases. At the end of each experiment, a thick layer of post-kinematic white sand was sprinkled on top of the model and then humidified to induce sand cohesion, allowing vertical sections to be sliced through the model. These cross-sections were cut parallel to the extension/shortening direction (perpendicular to the basement faults) across the central part of each model and labelled with numbers in order to localise them within the model.

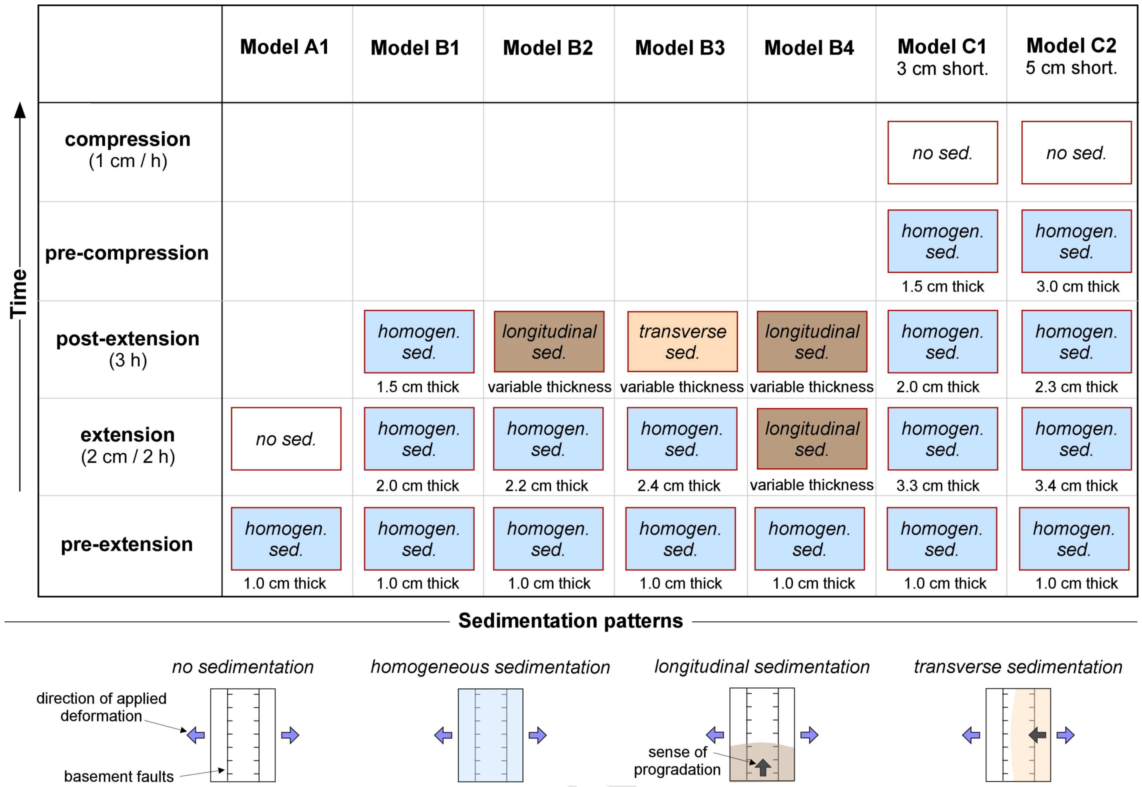

Fig. 4 Diagram showing the modelled tectonic phases through time (pre-extension, extension, post-extension, pre-compression, and compression), the applied sedimentation pattern (none, homogeneous, longitudinal, or transverse progradation), and the amount of shortening applied in the final phase of each model (for C1 and C2). The values (in cm) below the boxes indicate the mean thickness of the sedimentary layers for each phase.

4. Experimental results: the interactions between extension, diapirism, sedimentation, and compression

4.1. Model A1: extension phase without sedimentation

Model A1 represented the evolution of a basin during extension (a total extension of 2 cm or 4%) without sedimentation (Figs. 4 and 5). The hangingwall of the graben subsided homogeneously during extension at a rate of 1 cm/h (0.2 mm/yr in nature). After a total extension of 1 cm, newly formed small grabens developed on the pre-extension layer in the footwall of the basement faults and subparallel to their strike. On both footwalls, the grabens were located either close to the tip line of the basement faults (border grabens) or in the footwall interior (lateral grabens) (Fig. 5). These grabens were still extending at the end of the extensional phase (2 cm of extension).

The cross-sections sliced after applying extension showed roughly symmetric grabens affecting the pre-extension sedimentary unit above the silicone layer (Fig. 5). Along the edges of the basement graben, small border grabens showed rotation towards the main graben basin because of the drag folding of pre-extension beds above the basement faults. Both border and lateral grabens exhibited nucleation of small triangular reactive diapirs in their basal parts, similar to other previous analogue models (e.g., Dooley et al., 2005; Hudec and Jackson, 2007; Nalpas and Brun, 1993; Rowan et al., 1999; Vendeville and Jackson, 1992). Along the tip lines of the basement normal faults, a necking effect produced either a thinning of the silicone layer (only 0.47 cm thick) or its final welding (Fig. 5). The thickness of the silicone in the initial phase of this model (1 cm thick in the footwall and 2 cm thick in the hangingwall block) was not thick enough to avoid the welding caused by the subsidence of the hangingwall block and the related drag folding during extension. This has also been observed in previously published analogue models, such as those of Nalpas and Brun (1993), Jackson and Vendeville (1994), Vendeville et al. (1995) (their fig. 5), Dooley et al. (2003) (their figs 8 and 10), Dooley et al. (2005), Loncke et al. (2010) (their fig. 10), and Burliga et al. (2012).

The total subsidence measured in the central part of the hangingwall was 2.5 cm. This subsidence resulted from a combination of 80% of tectonic subsidence, associated with 2 cm of vertical displacement of the hangingwall during extension (Fig. 5), and 20% of silicone migration.

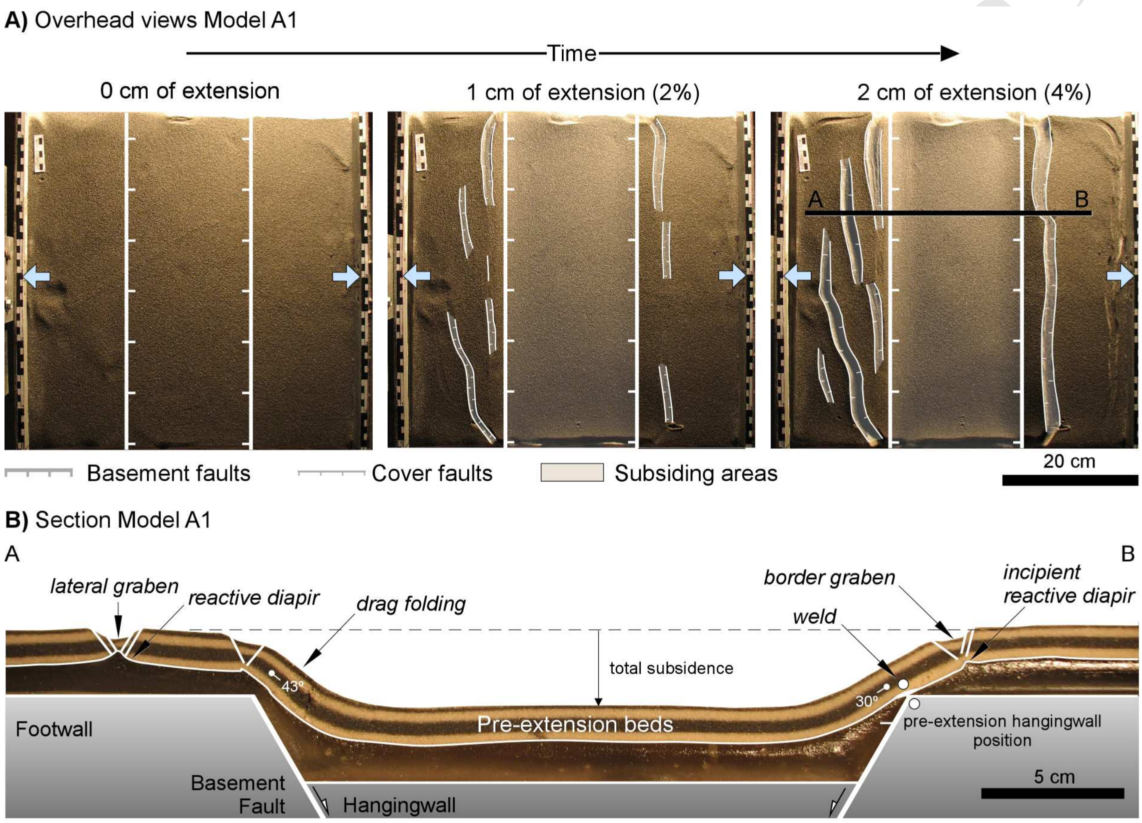

Fig. 5 (A) Overhead views of Model A1 (total extension = 2 cm) showing the distribution of several newly formed grabens in the pre-extension beds. (B) Model A1 section showing the geometry of grabens in the pre-extension beds bounded by two opposing normal faults rooted in incipient reactive diapirs. Post-kinematic sediments have been removed in the section view.

4.2. B-series models: extension and post-extension phases with variable sedimentation

Four models (B1, B2, B3, and B4 in Fig. 4) were developed using the same extension rate as that of Model A1 (1 cm/h for 2 h, with a total extension of 2 cm or 4%) and a post-extension phase of 3 h. The silicone layer in these models was thicker than in Model A1 (2 cm in the footwall and 3 cm in the hangingwall) to avoid welding on top of the footwall blocks, which would have hampered the formation and growth of diapiric structures. In models B1, B2, and B3, syn-extension homogeneous sediments were deposited in the main area of subsidence corresponding to the graben between the two conjugate basement faults. This sedimentation occurred at a rate equivalent to the accommodation rate (subsidence of central block plus silicone expulsion). During the post-extension phase, the models were subjected to different patterns of sedimentation (Fig. 4): homogeneous sedimentation for Model B1 (Fig. 6), longitudinal prograding sedimentation (parallel to the graben axis) in Model B2 (Fig. 7), and transverse prograding sedimentation (orthogonal to the basin axis) in Model B3 (Fig. 8). In contrast, Model B4 was run with longitudinal prograding sedimentation in both the extension and post-extension phases (Fig. 9).

Model B1 (Fig. 6), characterised by homogeneous sedimentation during both the extension and post-extension phases (Fig. 4), showed the development of elongated newly formed grabens in the footwall blocks, close to the tip lines of the basement faults, during the extension phase. Taking the results from Model A1 as a reference, these elongated grabens marked the locations of reactive diapirs beneath the pre-extension sand layers. This model, as well as other B-series models, showed how diapiric structures increased their level of maturation from reactive and active diapirism to passive diapiric phases. Thereby, during the post-extension phase of Model B1, the sedimentation in the central graben and the associated silicone migration enabled long and continuous reactive–active diapirs to transition to more mature diapiric structures with different geometries, as shown in cross-sections at the end of the post-extensional phase (Fig. 6B and C). The transition from reactive to passive diapirism through an active phase, which occurred when the pre-extension sand layers had thinned sufficiently to reach the threshold for forceful piercing (Vendeville and Jackson 1992), was recorded by the arching of both the pre-extension beds thinned during extension and the footwall domains (Fig. 6).

Diapirs on the left-hand side of Model B1 showed geometries similar to those of salt rollers (roller-like diapirs in Fig. 6). Salt rollers are immature structures developed in extensional settings and are defined as ridge-like diapirs, being asymmetrical in cross-section with a long gently dipping flank and a short steep scarp flank delineated by a normal fault (Bally, 1981; Brun and Mauduit, 2009; Jackson and Talbot, 1986; Quirk and Pilcher, 2012). The geometry of the diapir on the right-hand side of the model changed laterally from a roller-like diapir in section 25 (B–B' in Fig. 6) to a well-developed passive diapir with steep walls, a smooth basinward vergence, and incipient extrusion in section 38 (A–A' in Fig. 6). The silicone layer at the end of the experiment exceeded 2.2 cm in thickness in both footwall blocks, but only exceeded 1.7 cm along the central part of the hangingwall. The necking effect at the tip of the basement faults reduced the thickness of the silicone layer by up to 0.20–0.65 cm. The area balances of the silicone layer calculated in both sections 38 and 25 recorded similar reductions in silicone thickness (80% remaining) compared with the original silicone area. This indicates that silicone was expulsed in the extension direction with little or no migration along strike. The total subsidence measured in Model B1, 3.7 cm, resulted from a combination of tectonic subsidence and silicone expulsion (50% and 50%, respectively).

In Model B1, the migration of silicone towards the diapirs of the footwall domains tilted and folded the pre-extension sand layers, resulting in flaps flanking the diapiric structures (Dooley et al., 2005; Rowan et al., 2003; Saura et al., 2016; Schultz-Ela, 2003; Schultz-Ela et al., 1993) (Fig. 6). The outward flaps, in the footwall of both basement faults, had low dips that ranged from 8° to 16°. In contrast, in the hangingwall, the inward flaps were steeper, with a mean inclination between 24° and 30° close to the basement faults. In addition, the left-hand-side inward flap showed a 0.5-cm long uppermost segment dipping up to 38° in both sections 25 and 38 (Fig. 6C and Fig. 6B, respectively).

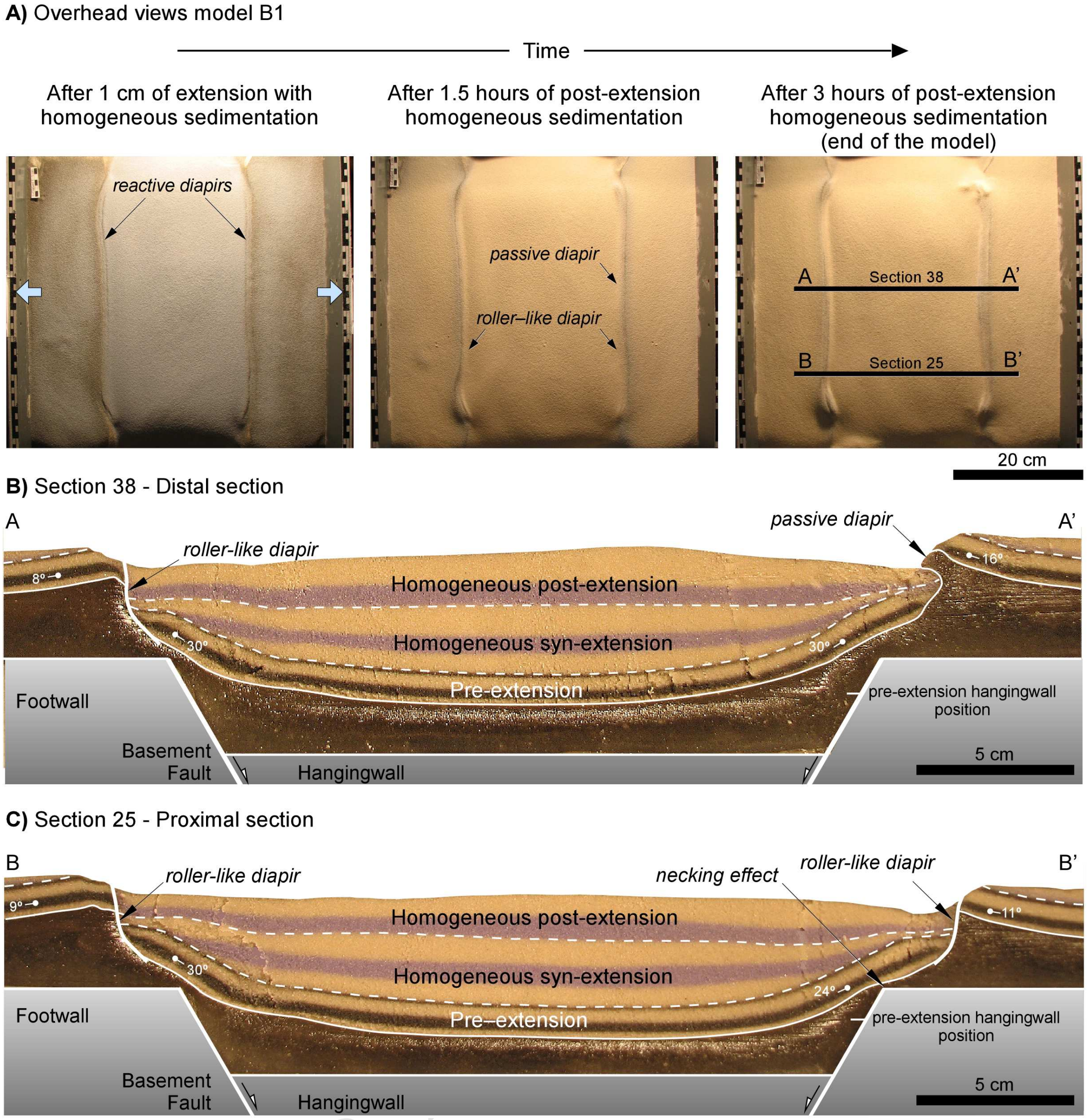

Fig. 6 Overhead views (A) and sections (B and C) showing the geometries resulting from Model B1. This model was characterised by an extensional phase (total extension = 2 cm) and a post-extensional phase (3 h) with homogeneous sedimentation during both phases. The thick white line marks the diapir wall acting as a normal fault. Post-kinematic sediments have been removed in the section view.

Model B2 (Fig. 7) was run with syn-extension homogeneous sedimentation followed by post-extension longitudinal sedimentary progradation (Fig. 4). The model displayed elongated newly formed grabens in the footwalls close to the main basement faults, with each of them being associated with reactive diapirs, as seen in Model B1 (Figs 6 and 7). The reactive diapirs developed during the extension phase, then evolved to become active and, finally, passive diapirs along the entire modelling device (Fig. 7). The proximal diapirs in Model B2 leaned inwards (Fig. 7C), with very steep walls and incipient silicone extrusions as the silicone migrated to the diapir. Towards the distal part of the model (Fig. 7B), the silicone extrusions and diapirs were wider and more mature, with proximal diapir walls being less than 0.9 cm wide, and distal diapir walls being more than 1.2 cm wide (Fig. 7). These differences in diapir width and silicone extrusion were partially due to the local thickness of the sedimentary pile and the silicone migration related to differential loading. The mean value of the syn-extension sedimentary succession along strike was around 2.6 cm, but the progradational post-extension sedimentary succession changed in thickness, being 3.5 times thinner in the distal domain than in the proximal domain (thicknesses of 0.45 cm and 1.5 cm, respectively).

At the end of the Model B2, the percentage of silicone preserved in the distal and proximal domains (67% and 60%, respectively) indicated a migration of silicone along the graben axis due to differential loading related to the longitudinal progradation of the post-extension sedimentary wedge. In this model, the welding of the pre-extension deposits against the tip line of the basement normal faults was strong in the proximal areas (0.2-cm-thick silicone compared with 0.6-cm-thick in the distal domain; Fig. 7), even reaching the complete welding stage. In Model B2, the outward flaps displayed dips ranging between 14° and 17° whereas the inward flaps dipped between 26° and 35° (Fig. 7), which were similar dip values to those observed in Model B1.

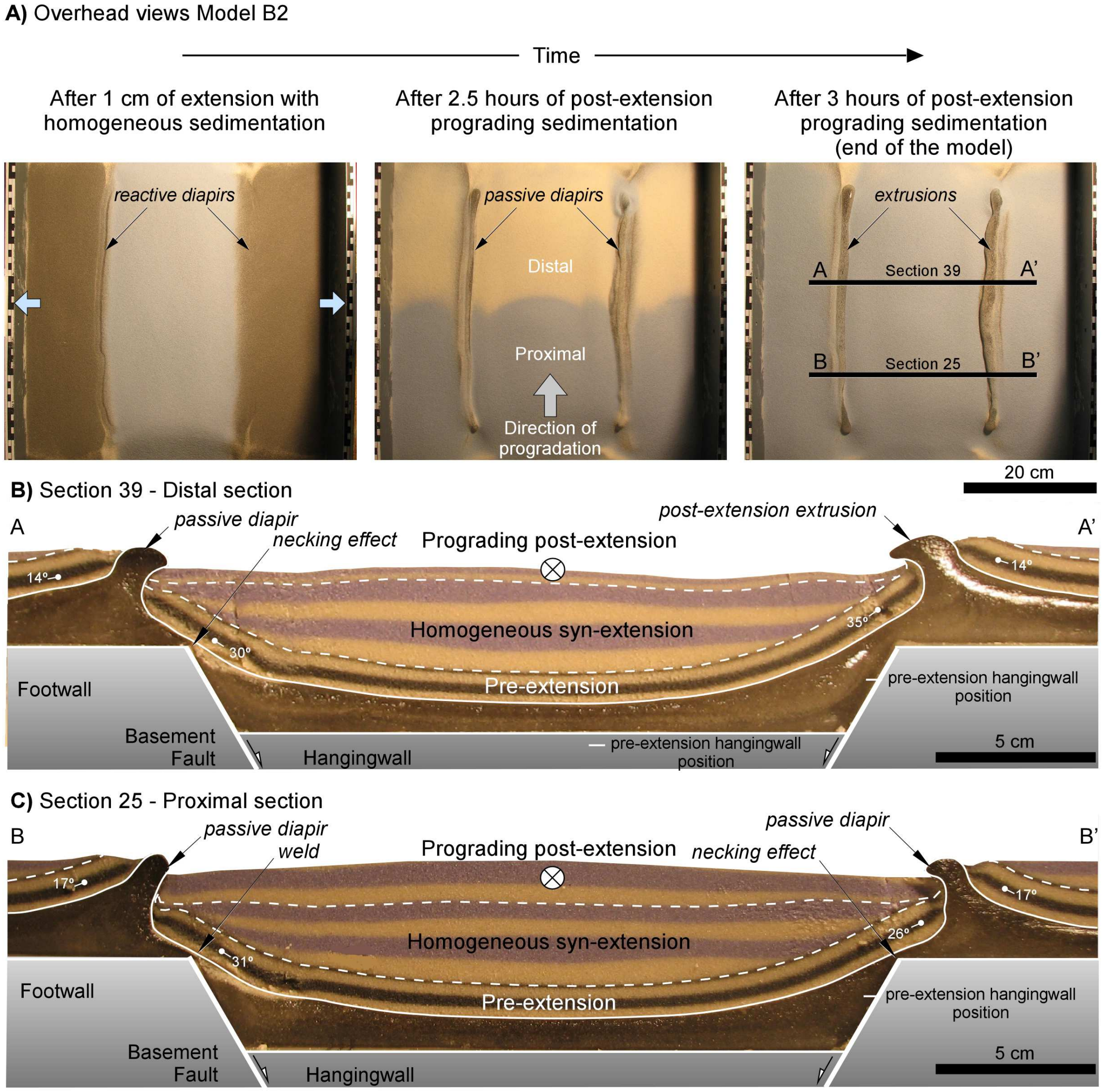

Fig. 7 Overhead views (A) and sections (B and C) showing the geometries resulting from Model B2. This model included an extensional phase (total extension = 2 cm) with homogeneous sedimentation and a post-extensional phase (3 h) with longitudinal prograding sedimentation. The diapir geometries varied laterally from the proximal (section 25) to the distal domains (section 39). Post-kinematic sediments have been removed in the section view.

Model B3 was run with syn-extension homogeneous sedimentation followed by post-extension transverse sedimentary progradation with the proximal domain being on the right-hand side of the model device (Figs 4 and 8). The extension phase reproduced extensional geometries comparable with those of models B1 and B2 (Fig. 8A). Across strike, Model B3 developed an asymmetric geometry during the post-extension phase, in contrast to models B1 and B2. At the end of the experiment, passive diapir walls in the proximal domain, where post-extension deposits were three times thicker than in the distal domain, were mature and characterised by very steep flanks in both sections shown in Figure 8B and C. In contrast, the diapiric structures developed in the distal domain were incipient roller-like diapirs, with a predominant right-dipping normal fault, laterally evolving to silicone walls that were less developed than in the proximal domain.

The final geometry of the silicone layer in Model B3 was asymmetric across the model, with a thinner silicone layer in the proximal domain (1.22 cm thick compared with 1.76 cm in the distal domain) on account of the transverse progradational deposits of the post-extension units and the resultant differential loading. In this model, the necking effects on top of the tip lines of the basement faults were limited (0.6-cm-thick silicone layer). The steepest pre-extension layering of the model corresponded to the inward flaps of the proximal domain with dips ranging from 80° to overturned (Fig. 8), whereas the inward flaps of the distal silicone walls ranged from 35° to 38°. The overturning, which reached 1 cm in length, was clearly a diapiric contribution as the only tectonic mechanism operating in Model B3 was extension.

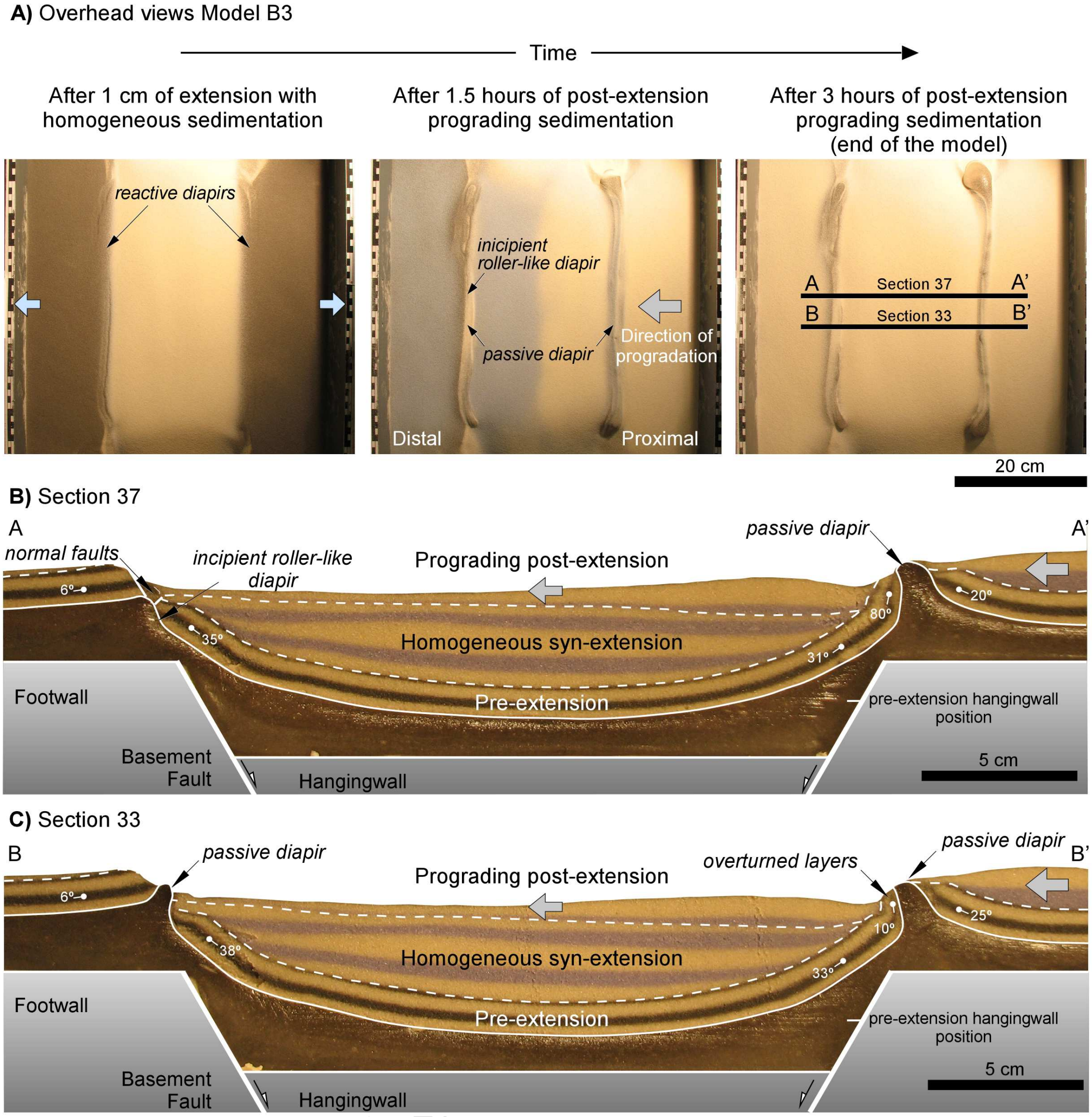

Fig. 8 Overhead views (A) and sections (B and C) showing the geometries resulting from Model B3. This model included an extensional phase (total extension = 2 cm) with homogeneous sedimentation and a post-extensional phase (3 h) with transverse prograding sedimentation. The diapir geometries of the proximal domains (right-hand sides of the model) differed from those of the distal domains (left-hand sides). Post-kinematic sediments have been removed in the section view.

Model B4 (Fig. 9) was run with both syn-extension and post-extension longitudinal sedimentary progradation (Fig. 4) and showed a final configuration that differed substantially from those of models B1, B2, and B3. During the extension phase, differential loading associated with longitudinal progradation caused the expulsion of silicone towards the distal domain and triggered the development of three distinctive features in Model B4 not observed in the other models (Fig. 9): i) the disruption of the two elongated grabens that characterised other B-series models, ii) the presence of a collapse fault developed in the proximal domain, and iii) the growth of an expulsion anticline (Fig. 9A).

At the end of the Model B4, after the post-extension phase characterised by the continuation of longitudinal progradation, the geometries of diapirs displayed marked differences when comparing the proximal and distal domains. The proximal domain of the model was characterised by <1-cm-wide well-developed extrusive diapirs oriented subvertically or slightly vergent towards the graben (Fig. 9C). The geometry of the silicone walls after the complete welding against the basement differed slightly from those of the other B-series models, with smooth folding of the inward flanks owing to local subsidence of the upper parts of the inward flanks within the silicone wall pedestal (Fig. 9C). In contrast, the distal region of the main basement graben was characterised by a much less evolved diapiric system, with stagnant reactive diapirs being developed during the extensional phase. The axial inflow of silicone to this area limited the subsidence of the hangingwall, preventing the required thinning of the pre-extension layers for the transition from the reactive to the active phase (Fig. 9B).

A comparison of the area balance of the silicone layer before and after the deposition of the prograding sequence showed a greater reduction in the proximal domain (about 47% remaining) than in the distal domain (nearly 70% remaining). These differences recorded the axial flow of the silicone from the proximal to the distal domain and the growth of an expulsion anticline from sections 35 to 38 (Fig. 9D). This expulsion anticline, which was bounded by the along-strike silicone walls, produced a compartmentalization of the silicone domain separating growing minibasins as well as controlling their size and the direction of their major axes. It is possible to infer from these results that a continuous progradation along the axes of the minibasins infilling the graben could produce either several of these orthogonal silicone walls (given sufficient available silicone) or a migrating silicone inflation (implying the depletion of the former silicone wall over time and the formation of complex patterns of minibasin sedimentary infill).

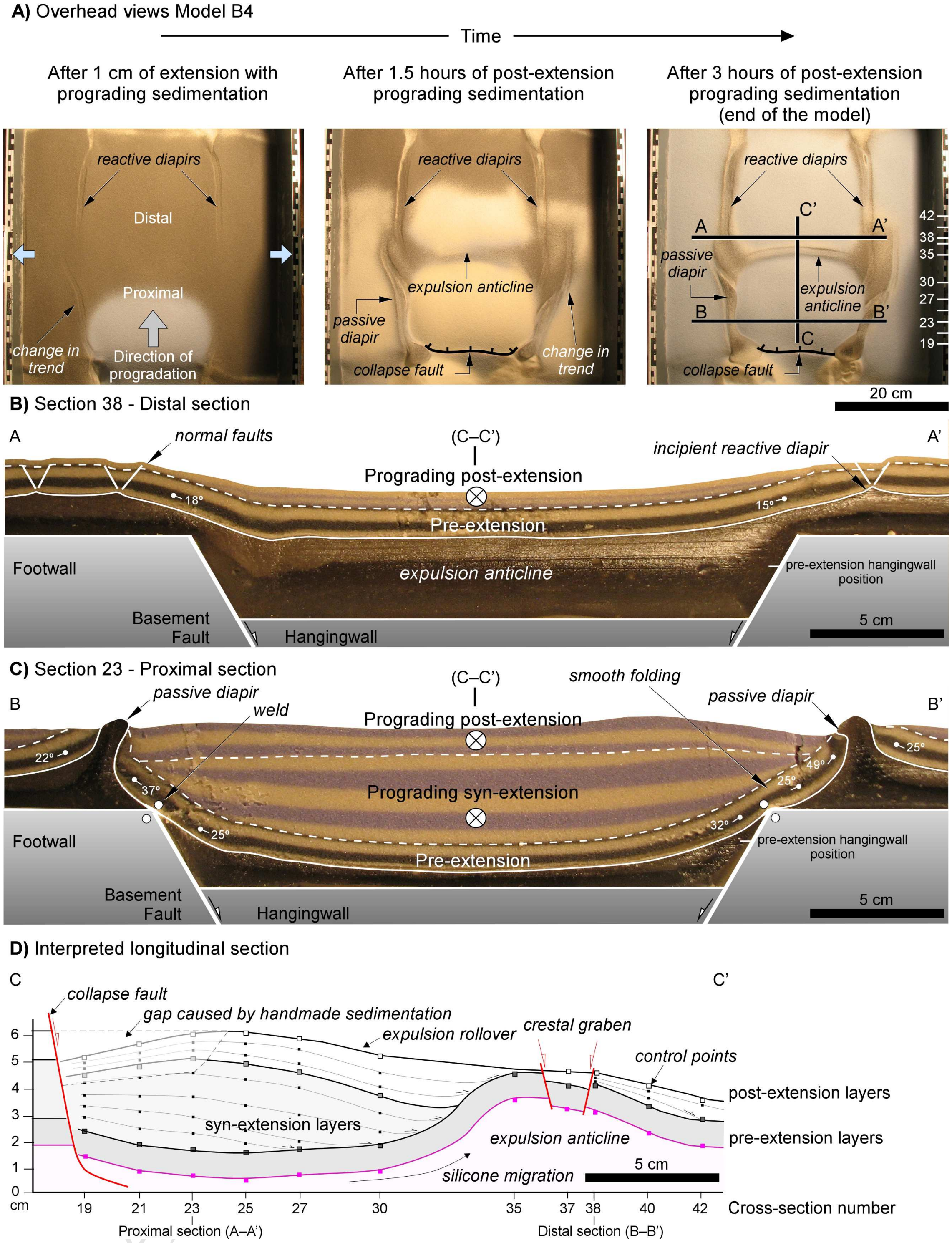

A) Overhead views Model B4
Time
After 1 cm of extension with prograding sedimentation
After 1.5 hours of post-extension prograding sedimentation
After 3 hours of post-extension prograding sedimentation (end of the model)
reactive diapirs
Distal
Proximal
change in trend
Direction of progradation
expulsion anticline
passive diapir
collapse fault
A
A'
B
B'
C
C'
42
38
35
30
27
23
19
20 cm
B) Section 38 - Distal section
normal faults
(C–C')
Prograding post-extension
incipient reactive diapir
18º
15º
Pre-extension
Footwall
expulsion anticline
pre-extension hangingwall position
Basement Fault
Hangingwall
5 cm
C) Section 23 - Proximal section
passive diapir
weld
smooth folding
22º
37º
25º
49º
32º
Prograding syn-extension
D) Interpreted longitudinal section
collapse fault
gap caused by handmade sedimentation
expulsion rollover
crestal graben
control points
post-extension layers
syn-extension layers
pre-extension layers
silicone migration
cm
Cross-section number
Proximal section (A–A')
Distal section (B–B')

Fig. 9 Overhead views (A) and sections (B and C) showing the geometries resulting from Model B4. This model included an extensional phase (total extension = 2 cm) and post-extensional phase (3 h) with longitudinal prograding sedimentation during both phases. Post-kinematic sediments have been removed in the section view. The longitudinal section from C to C' (D) was constructed by compiling the transverse sections from the model.

4.3. Models C1 and C2: extension and post-extension phases with homogeneous sedimentation and subsequent compression (6% and 10% shortening)

Models C1 and C2 (Fig. 10) used simple syn-rift and post-extension homogeneous sedimentation based on Model B1 (Fig. 4) and displayed compressional structures developed during basin inversion. Models C1 and C2 were performed with different amounts of post-diapiric and pre-compression sedimentation (1.5 and 3 cm, respectively) and with different applied shortening (3 and 5 cm, corresponding to 6% and 10%, respectively). The applied 6% of shortening (2.5 cm of uplift) did not fully invert the hangingwall in Model C1, whereas 10% of shortening (4 cm of uplift) produced a total positive inversion (pop-up structure) of the hangingwall in Model C2 (Fig. 10). Owing to the presence of non-deformable basement in the model, the upward movement of the hangingwall during compression reopened previously welded areas above the tip lines of the basement faults and facilitated a renewed flow of silicone towards the diapiric structures and footwall domains.

Model C1 was characterised by the positive tectonic inversion of the central graben hangingwall, by the gentle folding of the entire pre-, syn-, and post-rift sedimentary successions within the extensional minibasin, and by the rejuvenation of subvertical diapiric ridges along both footwall blocks (section 37 A–A’ in Fig. 10). An extreme thinning of the silicone layer occurred at the base of the extensional minibasin, giving an incomplete weld with a 0.1-cm-thick silicone remnant. The hangingwall pre-extension layers showed similar or slightly steeper dips of 30° to 49° compared with the purely extensional models (dips of 18° to 49°). However, the outward flaps of diapir silicone walls along the footwall blocks were somewhat steeper (up to 30° on the left-hand side and up to 36° on the right-hand side of the model, respectively) than similar geometries formed in the B-series models (between 8° and 17°). The thin pre-compression layers in Model C1 were deformed and thrusted on top of rejuvenated diapirs that showed steep to overturned flanks (Fig. 10). The compression event combined with moderately thick pre-compression beds permitted the complete breakup of the roof above the rejuvenated diapirs and the formation of syn-compression silicone extrusions. The vergence of silicone extrusion was away from the inverted central graben because of its higher elevation, in contrast to the extensional models, in which the topographic low was located in the subsiding central graben basin.

Model C2 was run with a pre-compression sand layer that was twice as thick as that in Model C1 (3 and 1.5 cm, respectively). After 5 cm of shortening, Model C2 showed positive inversion of the central graben and dome-shaped folding of the syn- and post-extension and pre-compression sedimentary successions above the pop-up basement structure (Fig. 10D). The thicker pre-compression layers in Model C2 were deformed mainly close to and above the rejuvenated diapirs. A large monocline, associated with a thrust fault, was observed in the pre-compression units on the left-hand side of the model, whereas the more evolved diapir on the right-hand side of the model produced a subvertical fold in the pre-compression layers (thrusted box-fold geometry). Outer-arc extension resulted in roof-collapse normal faults along the crest of the rejuvenated diapir ridge. However, the most noteworthy results were the full welding of both border silicone walls, resulting in detached silicone stocks, and the formation of a primary weld of the minibasin against the uplifted basement of the central graben (Fig. 10). The secondary weld located on the right-hand side of the model was a thrust weld, with the right-hand-side footwall succession being thrusted above younger rocks of the central minibasin; the thrust weld might also have been generated by the inversion of roller-like diapirs (see Dooley et al., 2005). Compared with C1, the pre-extension layers in C2 showed a steeper inclination that was achieved mostly around the time of or after the welding episode along the border silicone walls. The welding of the border diapirs and their subsequent buttressing resulted in an increase in the dips of the outward flaps (Fig. 10), which were steeper than 50° where the flanks were subparallel to the welded diapir walls. The inward flanks of the silicone diapir walls, delimiting the central graben minibasin, showed dips of 30°–40° but in some cases were very steep (75°) to overturned in their uppermost short segments close to the diapir wall (uppermost short segment length about 0.3 cm on the left-hand-side flank of the minibasin and 0.5 cm in the right-hand-side flank; Fig. 10).

Fig. 10 Overhead views (A and C) and sections (B and D) showing models C1 and C2. These models had an extensional phase (total extension = 2 cm), a post-extensional phase with homogeneous sedimentation, a pre-compression phase with homogeneous sedimentation of 1.5-cm thickness in Model C1 and 3-cm thickness in Model C2, and a final compression phase with a total amount of shortening of 3 cm (6%) in Model C1 and 5 cm (10%) in Model C2.

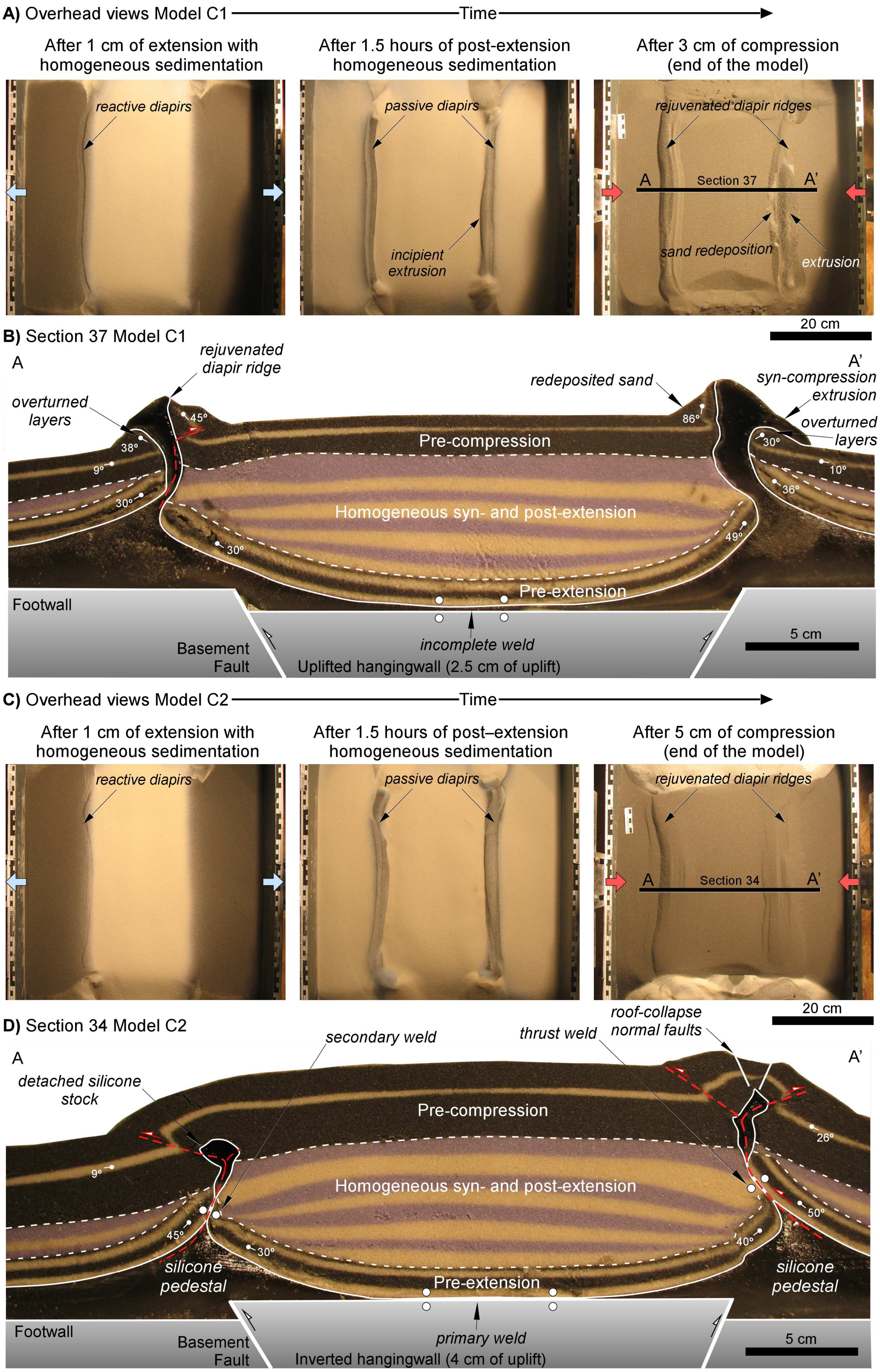

A) Overhead views Model C1
Time
After 1 cm of extension with homogeneous sedimentation
After 1.5 hours of post-extension homogeneous sedimentation
After 3 cm of compression (end of the model)
reactive diapirs
passive diapirs
incipient extrusion
rejuvenated diapir ridges
A
Section 37
A'
sand redeposition
extrusion
20 cm
B) Section 37 Model C1
A
rejuvenated diapir ridge
overturned layers
redeposited sand
A'
syn-compression extrusion
overturned layers
45º
38º
9º
30º
86º
30º
10º
36º
49º
30º
Pre-compression
Homogeneous syn- and post-extension
Pre-extension
Footwall
Basement Fault
incomplete weld
Uplifted hangingwall (2.5 cm of uplift)
5 cm
C) Overhead views Model C2
Time
After 1 cm of extension with homogeneous sedimentation
After 1.5 hours of post–extension homogeneous sedimentation
After 5 cm of compression (end of the model)
reactive diapirs
passive diapirs
rejuvenated diapir ridges
A
Section 34
A'
20 cm
D) Section 34 Model C2
A
detached silicone stock
secondary weld
thrust weld
roof-collapse normal faults
A'
Pre-compression
Homogeneous syn- and post-extension
Pre-extension
9º
45º
30º
26º
50º
40º
silicone pedestal
silicone pedestal
Footwall
Basement Fault
primary weld
Inverted hangingwall (4 cm of uplift)
5 cm

72

73

5. Discussion

5.1. The sedimentary contribution to diapiric growth in salt-related rift basins

As has been demonstrated by the use of analogue models and case studies since the early 1990s, extension is a mechanism that can readily trigger reactive, active, and passive diapirism in salt-related rift basins (Dooley et al., 2005; Duffy et al., 2012; Jackson and Vendeville, 1994; Kane et al., 2010; Koyi et al., 1993; Lewis et al., 2013; Nalpas and Brun, 1993; Pascoe et al., 1999; Schultz-Ela and Jackson, 1996; Vendeville and Jackson, 1992; Vendeville et al., 1995; Withjack and Callaway, 2000). Syn- to post-rift sedimentation and the different sedimentary patterns used for infilling the basin, however, control the further evolution of passive diapirism in our models (see model configurations in Fig. 4).

Syn-extension homogeneous sedimentation applied in models B1, B2, and B3 causes the formation of well-developed rectilinear reactive diapirs along the footwall blocks of basement faults (extensional overhead views in Figs 6, 7, and 8) that evolve to passive diapirs resulting in the formation of rectilinear silicone ridges. The diverse post-extension sedimentation applied to these models control the final diapiric geometry. Diapirs in Model B1 and in the proximal domains of models B2 and B3 are well-developed steep passive diapirs owing to the equilibrium between sedimentation rate and diapir growth velocity (Giles and Lawton, 2002; Talbot, 1995; Vendeville et al., 1993). The distal domain of Model B2 (Fig. 7B), with longitudinal post-extensional prograding sedimentation, shows significant silicone extrusion along the passive diapirs. These allochthonous bodies are able to expand on top of the hangingwall deposits because the post-extension sedimentation is too thin to compensate the growth of the diapirs (Koyi, 1998; Talbot, 1995; Vendeville and Jackson, 1992; Vendeville et al., 1993). The distal domains of Model B3 (Fig. 8B and C), with transverse post-extensional prograding sedimentation from right to left across the model, show poorly developed diapiric geometries, evolving from incipient roller-like diapirs to passive diapirs of smaller dimensions than those in the proximal domain.

Syn-extensional longitudinal prograding sedimentation applied in Model B4 (Fig. 9) causes the axial migration of silicone from the proximal domain to the distal domain, which, together with the limited amount of sand deposited during the late post-extension phase, limits the drag folding of pre-kinematic layers. Consequently, sufficient thinning of the pre-extension layers in the distal part of the model is not generated to allow a progression from incipient reactive diapiric structures to more evolved phases of diapirism. The longitudinal syn- and post-extensional prograding sedimentation of Model B4 also causes the growth of an expulsion anticline ahead of the prograding lobe that is perpendicular to the basement graben. Additionally, such sedimentation results in the development of discontinuous and non-rectilinear reactive diapirs that are diverted by silicone inflation (Fig. 9). We interpret the observed discontinuity as a result of the interaction between the regional extension and the local stress field associated with expulsion anticline growth caused by the thick and localised sedimentation of the syn-extensional sedimentary lobe (Gaullier and Vendeville, 2005; Sellier et al., 2013).

The salt migration resulting from the sedimentary load increases both the total and tectonic subsidence amounts, although its relative contribution is difficult to determine in subsidence analyses (Moragas et al., 2016). The comparison of models A1 and B1 allows the value of this salt migration and its contribution to tectonic subsidence to be quantified, taking into account the initial configuration of the models and their silicone thicknesses. In their respective final phases, Model A1 allows the tectonic (extension-related) subsidence at the end of extension to be isolated, whereas Model B1 allows both the tectonic (extension-related) and silicone migration (salt-migration-related) subsidence to be quantified for both extensional and post-extensional periods.

The total subsidence measured in the purely extensional Model A1 (i.e., without syn-extensional sedimentation) results from the sum of 80% of extension-related subsidence and 20% of salt-migration-related subsidence. These percentages change when both syn- and post-extensional sedimentation are applied (all B-series models). Calculations for Model B1 (Fig. 6C) yield 87% of extension-related and 13% of salt-migration-related contributions at the end of the extension. However, when the post-extension period of sedimentation is modelled, the contributions of the two mechanisms are very similar (ranging from 44% to 60% for the extension-related subsidence and from 40% to 56% for the salt-migration-related subsidence). This is because post-extension subsidence is strictly related to salt-migration in the models. These results should be applicable to subsidence analysis of sedimentary basins above thick salt layers, as in the Central High Atlas. However, one should take into account both the great differences in scale between the models and nature and the thermal subsidence associated with post-rift periods, as the reported in the Amezraï minibasin from the Central High Atlas (Moragas et al., 2016).

The results from the analogue modelling presented here show that sedimentation patterns are closely related not only to the evolution of diapiric structures and their geometries but also to the evolution of the diapiric basin as the configuration of the Central High Atlas reveals. Although transverse salt walls are exposed to a limited extent in the study area (see the geological map in Fig. 1), the combination of longitudinal syn- and post-extension prograding deposition generated a wide variation in the geometries of basin infill along the axis of the salt-related rift basin. This variation resulted in the growth of transverse salt walls at depth that can be correlated with the polygonal array of minibasins in the Central High Atlas.

5.2. Learning from analogue models applied to the shortened diapiric structures of the Central High Atlas in Morocco

Our models including shortening (Models C1 and C2) show that pre-compression salt structures have a substantial impact on the final configuration of an inverted salt basin, with the majority of compression-related deformation taking place in locations with a thin overburden, such as over the top of diapirs, as extensively documented in many studies (Burliga et al., 2012; Callot et al., 2007; Callot et al., 2012; Dooley et al., 2005, 2009; Letouzey et al., 1995; Nalpas et al., 1995; Rowan and Vendeville, 2006; Vially et al., 1994). As pointed out by previous studies, the anisotropy between the strong sedimentary pile and the weak silicone diapirs focuses the compressional strain in such diapiric structures.

Two main problems concerning the geometry of inverted salt-related rift basins, as here with particular respect to the case of the Central High Atlas, can now be examined in a more refined way by applying the results obtained from our analogue models. The first of these problems is how to differentiate between purely extensional and compressional imprints of salt-related features. The second one is how to infer the positions of buried basement faults beneath the thick sedimentary overburden and salt-bearing layers, as discussed below.

The comparison of extensional models B1 to B4 with compressional Model C1 (6% of shortening) and Model C2 (10% of shortening) allows distinguishing the effects of extension on the geometry of silicone ridges from the effects of compression. This is especially clear when comparing Models B1, C1 and C2, all of which were run using pre-, syn-, and post-extension homogeneous sedimentation (Fig. 4). To compare the shapes and dips of the flanks of the silicone diapirs, we plotted them at the same scale using the pre-extension layers forming the walls of the diapirs as reference lines (Fig. 11).

All purely extensional models display flaps with dips ranging from 8° to 17° in both footwall domains (outward flaps), whereas dips of the hangingwall flaps (inward flaps) are steeper, reaching 18°–40° and 25°–49° (Fig. 11). Data of Model B1 lay within these ranges, with 8°–11° in the footwalls and 30° for both sides of the hangingwall (Fig. 11). In contrast, the inverted models show an outward rotation of the outward flaps, with dips of 30° and 36° in Model C1 (6% shortening) and with the steepest outward flaps in Model C2 (10% shortening) reaching 45° and 50°. The evolution of the geometries of pre-kinematic beds in Fig. 11 shows how increasing shortening causes a steepening of extensional diapir flaps (mainly related to the footwall domains), whereas hangingwall flaps show dips in the same range as those of the extensional models, between 18° and 49°. According to our models, which were set up with the minimum thickness of silicone needed to develop diapirs, all footwall flanks dipping more than 17° need the contribution of compression to develop. Thus, our models show that the tectonic inversion produces a greater steepening in the outward flaps and a smaller steepening along the flanks of the minibasin. The models also show short segments with overturning in the inward flaps, as observed in both flanks of the Tazoult salt wall in the Central High Atlas (Fig. 12). That being said, the inward flap of the Tazoult salt wall shows a greater length and steeper inclination than that observed in any of our models, including those with compression. A possible explanation for this could be that a greater amount of salt migration would generate the ~80° dip observed in the southern flap of the Tazoult salt wall.

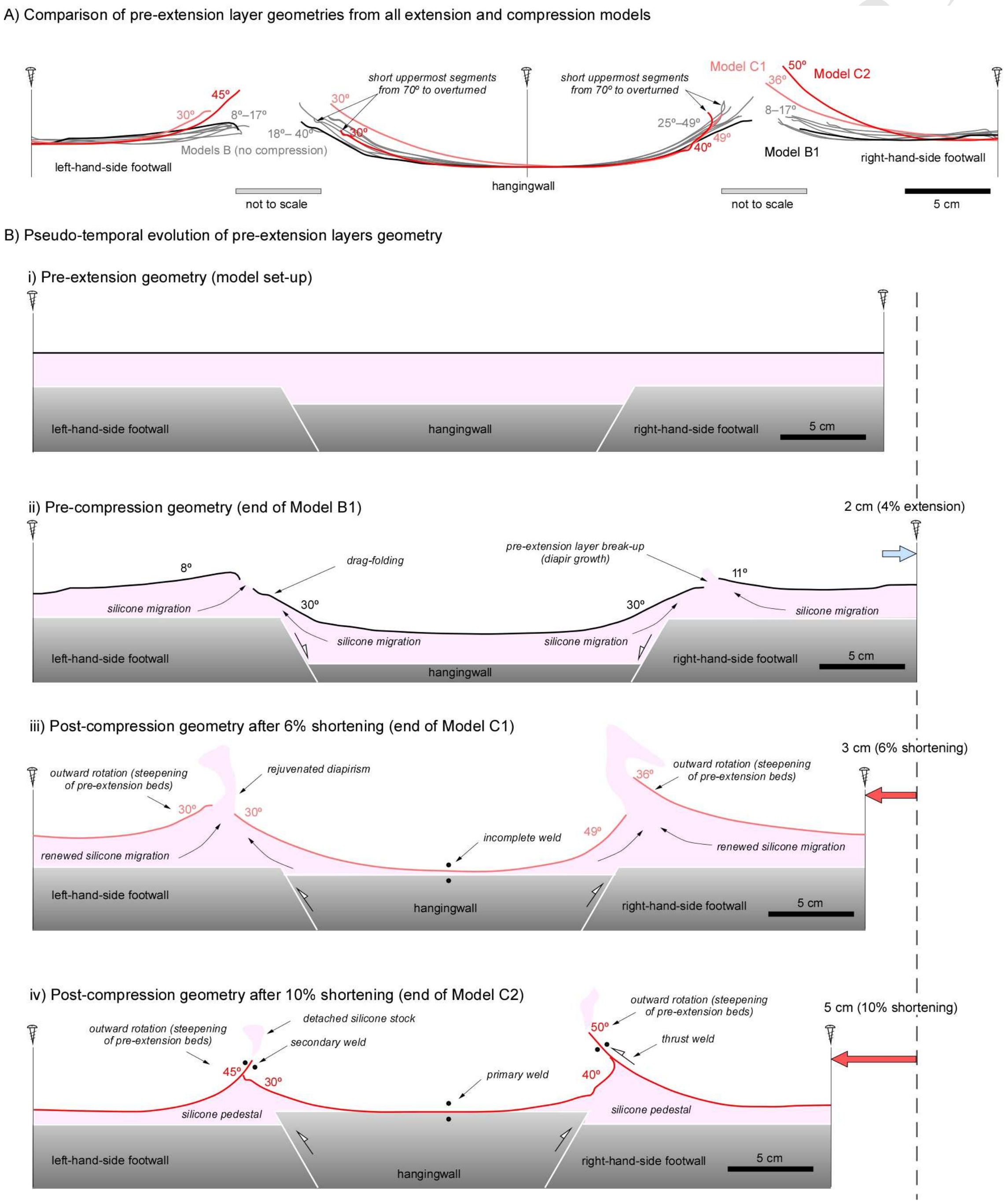

Fig. 11 (A) Comparison of pre-extension layer geometries from purely extensional models and models including 6% and 10% of compression. Compression causes the strongest steepening of pre-extension layers in the footwall domains. (B) Pseudo-temporal evolution of pre-extension layer geometry from extension through to 10% of shortening. The vertical scale equals the horizontal scale for all diagrams in both (A) and (B).

For the Tazoult and Jbel Azourki diapirs, the positions of basement faults in the cross-sections were inferred based on thickness variation between the two flanks of these diapiric salt walls (ridges). However, the positions and geometries of these faults at depth are imprecise, and the tip lines of the faults were placed directly under the diapir walls cropping out at the surface (Fig. 1; Martín-Martín et al., 2016). In contrast, according to our results and those of previously published models (e.g., Dooley et al., 2005), diapiric structures develop mostly in the footwalls of the basement normal faults and away from their tip lines. On the basis of our modelling, we propose a new cross-section in which the Tazoult and Jbel Azourki diapirs are located in the footwall domains of the basement normal faults that bound the Amezraï minibasin (compare Figs 1C and 12C).

The final geometry of diapirs after the shortening overprinting is another outcome from modelling that can be applied to better discriminate between extensional and compressional geometries, as observed for Models C1 and C2 (Figs 11 and 12). Our results show that passive diapirs formed during extension are tightened during subsequent compression, with reductions in diapir width ranging from 32% to 72% in Model C1 with 6% of shortening. These pre-existing diapirs are completely welded in Model C2 with 10% of shortening. In addition, the tightening and welding of diapirs may create a thrust weld, moving the extensional footwall overburden above the thicker extensional hangingwall post-silicone sedimentary pile. These results are consistent

229 with field observations in the Tazoult and Jbel Azourki diapir walls, which, under a
230 regional shortening of 10.4% (Martín-Martín et al., 2016), are completely welded in
231 areas where there have been no magmatic intrusions or slivers of Hettangian carbonates.

232

233 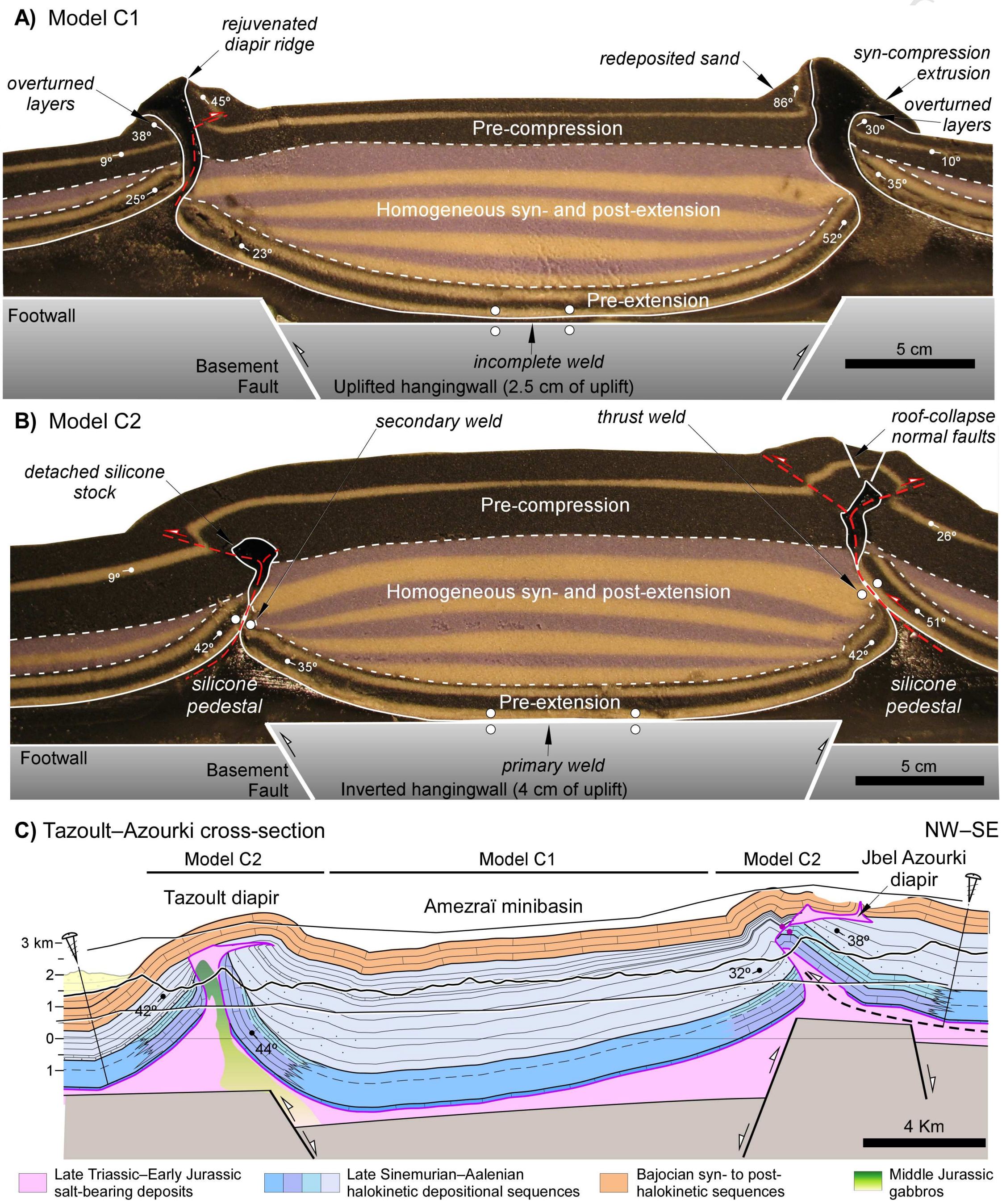

Fig. 12 Sections from Model C1 (A) and Model C2 (B), showing the main sand units according to the timing of deposition (pre-, syn-, and post-extension, and pre-compression). (C) A newly proposed cross-section from the Tazoult–Jbel Azourki transect (modified from Martín-Martín, et al., 2016; Fig. 1) with diapirs relocated on the footwalls of basement normal faults and black bars on top referring to geometries comparable to the corresponding analogue models. The thin black lines indicate the currently exposed structural levels and topography. The lateral facies change from the oldest halokinetic depositional sequences represents the transition from shallow-marine (light blue) to deep-marine (dark blue) deposits as recently reported in the Central High Atlas diapiric structures by Joussiaume (2016), Malaval (2016), Martín-Martín et al. (2016), Teixell et al. (2017), and Vergés et al. (2017).

6. Conclusions

Our physical models were designed to refer to the main feature of the Central High Atlas, namely, with a minimum salt-layer thickness of around 1.5 km. The presented models indicate a close interaction between tectonics, sedimentation, and diapirism in salt-related rift basins. Once extension-driven diapirism in the models begins, governed by the geometry of the fault system, the syn- and post-extension sedimentary patterns have a major influence on the evolution of such diapirism and on the configuration of the modelled basin.

In the models, syn-extension homogeneous sedimentation enhances the mobilisation of silicone towards growing diapirs, resulting in the development of passive diapiric ridges along the footwalls of the basement faults. Post-extension longitudinal and transverse sedimentary progradations cause variations in the diapiric geometries along the direction of progradation. Well-developed passive diapirs with vertical walls grow in the proximal domains, where sedimentation rates and diapir growth rates are in equilibrium. In contrast, silicone extrusions or poorly developed diapiric structures evolve in the distal domains, where sedimentation rates are lower than diapiric growth rates.

Syn- and post-extension longitudinal sedimentary progradation causes a substantial migration of silicone from proximal to distal domains of the prograding system, resulting in the growth of an expulsion anticline that hampers the progression of reactive diapirs to more evolved diapiric phases in the distal part of the models.

Tectonic inversion of the models triggers the following: i) the steepening of the outward flaps of pre-compression silicone diapir walls, with dips increasing from 8°–17° prior to compression to 30°–50° after compression; ii) the reopening of the silicone migration network by thrusting welds off the sub-silicone basement; and iii) the tightening of the silicone diapir walls and their final welding when shortening reaches ~10%.

The modelling results provide insights into the natural example of the Central High Atlas diapiric province in Morocco, as follows: a) the polygonal array of minibasins of the Central High Atlas is inferred to be a result of the growth of transverse salt walls associated with the syn- and post-extension longitudinal sedimentary progradation of the Early and Middle Jurassic; b) the Alpine Orogeny contributed to the steepening of the outward flaps of the Tazoult and Jbel Azourki diapirs, whereas the flanks of the Amezraï minibasin appear to have been only slightly deformed during shortening; c) the inferred basement normal faults in the Tazoult–Jbel Azourki transect can be redrawn to adjust them with respect to the diapir walls located in their footwalls instead of directly above their tip lines; and d) tectonic subsidence in salt-related rift basins, such as the Central High Atlas, includes a salt-migration-related subsidence component as high as

40%–56% of the total tectonic subsidence, which hampers the calculationof extensional factors.

7. Acknowledgements

This study was part of a collaborative research project funded by Statoil Research Centre, Bergen (Norway), and by the CSIC-FSE 2007-2013 JAE-Doc postdoctoral research contract (E.S.). The Spanish Ministry of Education and Science provided additional funding (MEC) through the projects Intramural Especial (CSIC 201330E030 and CSIC 201530E082) and MITE (CGL 2014-59516). We are grateful to Statoil for its support and permission to publish this study. Special thanks are due to J.-J. Kermarrec and Pascal Rolland for their valuable technical assistance and availability during model development in the Experimental Tectonics Laboratory of Géosciences Rennes (Université de Rennes 1, France). The authors acknowledge the use of the Move Software Suite granted by Midland Valley's Academic Software Initiative. This paper benefited from constructive reviews from Tim Dooley, Chris Talbot, Gael Lymer and Editor Enrique Gomez-Rivas.

8. References

Arboleya, M.L., Teixell, A., Charroud, M., Julivert, M., 2004. A structural transect through the High and Middle Atlas of Morocco. Journal of African Earth Sciences 39, 319-327.

Ayarza, P., Alvarez-Lobato, F., Teixell, A., Arboleya, M.L., Tesón, E., Julivert, M., Charroud, M., 2005. Crustal structure under the central High Atlas Mountains (Morocco) from geological and gravity data. Tectonophysics 400, 67–84.

Bally, A.W., 1981. Thoughts on the tectonics of folded belts, Geological Society Special Publication, pp. 13–32.

Baudon, C., Fabuel-Perez, I., Redfern, J., 2009. Structural style and evolution of a late Triassic rift basin in the Central High Atlas, Morocco: Controls on sediment deposition. Geological Journal 44, 677-691.

Beauchamp, W., Allmendinger, R.W., Barazangi, M., Demnati, A., El Alji, M., Dahmani, M., 1999. Inversion tectonics and the evolution of the High Atlas Mountains, Morocco, based on a geological-geophysical transect. Tectonics 18, 163-184.

Bouchouata, A., 1994. La ride de Talmest-Tazoult (Haut Atlas Central Maroc), lithostratigraphie, biostratigraphie et relations tectonique-sédimentation au cours du Jurassique. Strata, série 2 (memoires) 25, 219.

Bouchouata, A., Canerot, J., Souhel, A., Almeras, Y., 1995. Jurassic sequence stratigraphy and geodynamic evolution in the Talmest-Tazoult area, Central High Atlas, Morocco. Comptes Rendus de l'Académie des Sciences 320, 749–756.

Brun, J.P., Fort, X., 2004. Compressional salt tectonics (Angolan margin). Tectonophysics 382, 129–150.

Brun, J.P., Mauduit, T.P.O., 2009. Salt rollers: Structure and kinematics from analogue modelling. Marine and Petroleum Geology 26, 249–258.

Burliga, S., Koyi, H.A., Chemia, Z., 2012. Analogue and numerical modelling of salt supply to a diapiric structure rising above an active basement fault. Geological Society, London, Special Publications 363, 395–408.

Callot, J.P., Jahani, S., Letouzey, J., 2007. The role of pre-existing diapirs in fold and thrust belt development, in: Lacombe, O.L., J.; Roure, F.; Vergés, J. (Ed.), Thrust Belts and Foreland Basins From Fold Kinematics to Hydrocarbon Systems., pp. 309–326.

Callot, J.P., Trocmé, V., Letouzey, J., Albouy, E., Jahani, S., Sherkati, S., 2012. Pre-existing salt structures and the folding of the Zagros Mountains. Geological Society, London, Special Publications 363, 545–561.

Courel, L., Aït Salem, H., Benaouiss, N., Et-Touhami, M., Fekirine, B., Oujidi, M., Soussi, M., Tourani, A., 2003. Mid-Triassic to Early Liassic clastic/evaporitic deposits over the Maghreb Platform. Palaeogeography, Palaeoclimatology, Palaeoecology 196, 157-176

Davy, P., Cobbold, P.R., 1991. Experiments on shortening of a 4-layer model of the continental lithosphere. Tectonophysics 188, 1–25.

Domènech, M., Teixell, A., Babault, J., Arboleya, M.-L., 2015. The inverted Triassic rift of the Marrakech High Atlas: A reappraisal of basin geometries and faulting histories. Tectonophysics 663, 177-191.

Dooley, T., Hudec, M.R., 2017. The effects of base-salt relief on salt flow and suprasalt deformation patterns - Part 2: Application to the eastern Gulf of Mexico. Interpretation 5, 25–38.

Dooley, T., Hudec, M.R., Carruthers, D., Jackson, M.P.A., Luo, G., 2017. The effects of base-salt relief on salt flow and suprasalt deformation patterns - Part 1: Flow across simple steps in the base of salt. Interpretation 5, 1–23.

Dooley, T., McClay, K.R., Hempton, M., Smit, D., 2005. Salt tectonics above complex basement extensional fault systems: Results from analogue modelling, pp. 1631–1648.

Dooley, T., McClay, K.R., Pascoe, R., 2003. 3D analogue models of variable displacement extensional faults: applications to the Revfallet Fault system, offshore mid-Norway. Geological Society, London, Special Publications 212, 151–167.

Dooley, T.P., Jackson, M.P.A., Hudec, M.R., 2009. Inflation and deflation of deeply buried salt stocks during lateral shortening. Journal of Structural Geology 31, 582–600.

Dooley, T.P., Schreurs, G., 2012. Analogue modelling of intraplate strike-slip tectonics: A review and new experimental results. Tectonophysics 574–575, 1–71.

Duffy, O.B., Gawthorpe, R.L., Docherty, M., Brocklehurst, S.H., 2012. Mobile evaporite controls on the structural style and evolution of rift basins: Danish Central Graben, North Sea. Basin Research 24, 1-21.

Ellouz, N., Patriat, M., Gaulier, J.-M., Bouatmani, R., Sabounji, S., 2003. From rifting to Alpine inversion: Mesozoic and Cenozoic subsidence history of some Moroccan basins. Sedimentary Geology 156, 185–212.

Ettaki, M., Ibouh, H., Chellaï, E.H., Milhi, A., 2007. Liassic diapiric structures from the Central High Atlas, Morocco; Ikerzi ride example. Africa Geoscience Review 14, 79–93.

Faugère, E., Brun, J.P., 1984. Modélisation expérimentale de la distension continentale. Compte-Rendus de l'Académie des Sciences de Paris 299, 365–370.

Fort, X., Brun, J.P., Chauvel, F., 2004. Salt tectonics on the Angolan margin, synsedimentary deformation processes. AAPG Bulletin 88, 1523–1544.

Frizon de Lamotte, D., Bezar, B.S., Bracène, R., Mercier, E., 2000. The two main steps of the Atlas building and geodynamics of the western Mediterranean. Tectonics 19, 740–761.

Frizon de Lamotte, D., Leturmy, P., Missenard, Y., Khomsi, S., Ruiz, G., Saddiqi, O., Guillocheau, F., Michard, A., 2009. Mesozoic and Cenozoic vertical movements in the Atlas system (Algeria, Morocco, Tunisia): An overview. Tectonophysics 475, 9–28.

Frizon de Lamotte, D., Zizi, M., Missenard, Y., Hafid, M., Azzouzi, M., Maury, R.C., Charrière, A., Taki, Z., Benammi, M., Michard, A., 2008. The Atlas System, Continental Evolution: The Geology of Morocco, pp. 133-202.

Gaullier, V., Vendeville, B.C., 2005. Salt tectonics driven by sediment progradation: Part II - Radial spreading of sedimentary lobes prograding above salt. AAPG Bulletin 89, 1081–1089.

Ge, H., Jackson, M.P.A., Vendeville, B.C., 1997a. Kinematics and dynamics of salt tectonics driven by progradation. AAPG Bulletin 81, 398–423.

Ge, H., Jackson, M.P.A., Vendeville, B.C., Maler, M.O., Handschy, J.W., 1997b. Deformation of prograding wedges over a ductile layer - Applications of physical models to geologic examples. Gulf Coast Association of Geological Societies Transactions 47, 177–184.

Giles, K.A., Lawton, T.F., 2002. Halokinetic sequence stratigraphy adjacent to the El Papalote diapir, Northeastern Mexico. AAPG Bulletin 86, 823–840.

Graveleau, F., Malavieille, J., Dominguez, S., 2012. Experimental modelling of orogenic wedges: A review. Tectonophysics 538–540, 1–66.

Grélaud, C., Razin, P., Joussiaume, R., Malaval, M., Vergés, J., Saura, E., Martín-Martín, J.D., Moragas, M., Hunt, D., Messager, G., 2014. Diapiric control on Jurassic carbonate systems of the High Atlas Basin, Morocco, AAPG Annual Meeting, Houston, Texas.

Guerra, M.C.M., Underhill, J.R., 2012. Role of halokinesis in controlling structural styles and sediment dispersal in the Santos Basin, offshore Brazil. Geological Society, London, Special Publications 363, 175–206.

Hailwood, E.A., Mitchell, J.G., 1971. Palaeomagnetic and Radiometric Dating Results from Jurassic Intrusions in South Morocco. Geophysical Journal International 24, 351-364.

Hubbert, M.K., 1937. Theory of scale models as applied to the study of geological structures. Geological Society of America Bulletin 48, 1459-1520.

Hudec, M.R., Jackson, M.P.A., 2007. Terra infirma: Understanding salt tectonics. Earth-Science Reviews 82, 1–28.

Ibouh, H., Charrière, A., Michard, A., 2011. Middle Jurassic unsteady sedimentation in the High Atlas Basin (Imilchil area, Morocco) controlled by halokinetic and regional vertical movements. AAPG Search and Discovery #90137.

Jackson, M.P.A., Talbot, C.J., 1986. External shapes, strain rates, and dynamics of salt structures. Geological Society of America Bulletin 97, 305–323.

Jackson, M.P.A., Vendeville, B.C., 1994. Regional extension as a geologic trigger for diapirism. Geological Society of America Bulletin 106, 57–73.

Jenny, J., Le Marrec, A., Monbaron, M., 1981. Middle Jurassic red beds of central High Atlas (Morocco): lithostratigraphic correlations, dating data and tectono-sedimentary framework. Bulletin, Societe Geologique de France 23, 627-639.

Jossen, J.A., Couvreur, G., 1990. Carte Géologique du Marroc, feuille Zawyat Ahançal, Notes et Memoires du Service Géologique du Maroc (355).

Joussiaume, R., 2016. "Les relations entre diapirisme et sédimentation: Exemple du Jurassique moyen de la région d'Imilchil, Haut-Atlas central, Maroc". (The relationships between diapirism and sedimentation: An example from the Middle Jurassic of the Imilchil area, Central High-Atlas, Morocco.). Université Bordeaux-Montaigne Pessac, France.

Kane, K.E., Jackson, C.A.L., Larsen, E., 2010. Normal fault growth and fault-related folding in a salt-influenced rift basin: South Viking Graben, offshore Norway. Journal of Structural Geology 32, 490–506.

Koyi, H., 1996. Salt flow by aggrading and prograding overburdens. Geological Society, London, Special Publications 100, 243–258.

Koyi, H., 1997. Analogue Modelling: From a qualitative to a quantitative technique - a historical outline. Journal of Petroleum Geology 20, 223–238.

Koyi, H., 1998. The shaping of salt diapirs. Journal of Structural Geology 20, 321–338.

Koyi, H., Jenyon, M.K., Petersen, K., 1993. The effect of basement faulting on diapirism. Journal of Petroleum Geology 16, 285–312.

Krantz, R.W., 1991. Measurements of friction coefficients and cohesion for faulting and fault reactivation in laboratory models using sand and sand mixtures. Tectonophysics 188, 203–207.

Krézsek, C., Adam, J., Grujic, D., 2007. Mechanics of fault and expulsion rollover systems developed on passive margins detached on salt: Insights from analogue modelling and optical strain monitoring, pp. 103–121.

Laville, E., Harmand, C., 1982. Magmatic and tectonic evolution of Mesozoic intracontinental basin High- Atlas Mountains, Morocco: a model of synsedimentary anorogenic intrusions linked to strike slip faults. Bulletin de la Société Géologique de France 24, 213–227.

Laville, E., Lesage, J.-L., Seguret, M., 1977. Geometrie, cinematique (dynamique) de la tectonique atlasique sur le versant sud du Haut Atlas marocain; apercu sur les tectoniques hercyniennes et tardi-hercyniennes. Bulletin de la Societe Geologique de France Series 7 Vol. XIX, 527-539.

Laville, E., Piqué, A., 1992. Jurassic penetrative deformation and Cenozoic uplift in the Central High Atlas (Morocco): A tectonic model. structural and orogenic inversions. Geologische Rundschau 81, 157-170.

Laville, E., Pique, A., Amrhar, M., Charroud, M., 2004. A restatement of the Mesozoic Atlasic Rifting (Morocco). Journal of African Earth Sciences 38, 145-153.

Letouzey, J., Colletta, B., Vially, R., Chermette, J.C., 1995. Evolution of Salt-Related Structures in Compressional Settings, in: Jackson, M.P.A., Roberts, D.G., Snelson, S. (Eds.), AAPG Memoir 65 on Salt Tectonics: a global perspective, pp. 41–60.

Lewis, M.M., Jackson, C.A.L., Gawthorpe, R.L., 2013. Salt-influenced normal fault growth and forced folding: The Stavanger Fault System, North Sea. Journal of Structural Geology 54, 156–173.

Loncke, L., Vendeville, B.C., Gaullier, V., Mascle, J., 2010. Respective contributions of tectonic and gravity-driven processes on the structural pattern in the Eastern Nile deep-sea fan: insights from physical experiments. Basin Research 22, 765-782.

Malaval, M., 2016. "Enregistrement sédimentaire de l'activité diapirique associée à la ride du Jbel Azourki, Haut Atlas central, Maroc: Impact sur la géométrie des dépôts et la distribution des faciès des systèmes carbonatés et mixtes du Jurassique inférieur". (Synsedimentary record of diapiric activity related to the Jbel Azourki ridge, Central High Atlas, Morocco: Impact on depositional geometries and facies distribution of the Lower Jurassic carbonate and mixed systems.). Université Bordeaux-Montaigne Pessac, France.

Martín-Martín, J.D., Vergés, J., Saura, E., Moragas, M., Messager, G., Baqués, V., Razin, P., Grélaud, C., Malaval, M., Joussiaume, R., Casciello, E., Cruz-Orosa, I., Hunt, D.W., 2016. Diapiric growth within an Early Jurassic rift basin: the Tazoult salt wall (Central High Atlas, Morocco). Tectonics 35, 1–31.

Mattauer, M., Tapponier, P., Proust, F., 1977. Sur les mécanismes de formation des chaines intracontinentales: L'exemple des chaines atlasiques du Maroc. Bull. Soc. Géol. France 77 (7), 521-526.

McClay, K., 1996. Recent advances in analogue modelling: Uses in section interpretation and validation, Geological Society Special Publication, pp. 201–225.

McClay, K., Dooley, T., Lewis, G., 1998. Analog modeling of progradational delta systems. Geology 26, 771–774.

McClay, K., Dooley, T., Zamora, G., 2003. Analogue models of delta systems above ductile substrates, Geological Society Special Publication, pp. 411–428.

Michard, A., Ibouh, H., Charrière, A., 2011. Syncline-topped anticlinal ridges from the High Atlas: A Moroccan conundrum, and inspiring structures from the Syrian Arc, Israel. Terra Nova 23, 314–323.

Milhi, A., Ettaki, M., Chellai, E.H., Hadri, M., 2002. The lithostratigraphic formations of moroccan jurassic central High-Atlas: Interelationships and paleogeographic reconstitution. Revue de Paleobiologie 21, 241–256.

Moragas, M., Vergés, J., Saura, E., Martín-Martín, J.-D., Messager, G., Merino-Tomé, Ó., Suárez-Ruiz, I., Razin, P., Grélaud, C., Malaval, M., Joussiaume, R., Hunt, D.W., 2016. Jurassic rifting to post-rift subsidence analysis in the Central High Atlas and its relation to salt diapirism. Basin Research, 1–27.

Nalpas, T., Brun, J.P., 1993. Salt flow and diapirism related to extension at crustal scale. Tectonophysics 228, 349–362.

Nalpas, T., Le Douaran, S., Brun, J.-P., Unternehr, P., Richert, J.-P., 1995. Inversion of the Broad Fourteens Basin (offshore Netherlands), a small-scale model investigation. Sedimentary Geology 95, 237–250.

Oujidi, M., Courel, L., Benaouiss, N., El Mostaine, M., El Youssi, M., Et Touhami, M., Ouarhache, D., Sabaoui, A., Tourani, A., 2000. Triassic series of Morocco: stratigraphy, palaeogeography and structuring of the southwestern Peri-Tethyan platform. An overview, in: Crasquin-Soleau, S., Barrier, E. (Eds.), Peri-Tethys Memoir 5: New data on Peri-Tethyan sedimentary basins. Mémoires du Muséum National d´Histoire Naturelle, Paris, pp. 23-38.

Pascoe, R., Hooper, R., Storhaug, K., Harper, H., 1999. Evolution of extensional styles at the southern termination of the Nordland Ridge, Mid-Norway: A response to variations in coupling above Triassic salt, Petroleum Geology Conference Proceedings, pp. 83–90.

Pierre, A., Durlet, C., Razin, P., Chellai, E.H., 2010. Spatial and temporal distribution of ooids along a Jurassic carbonate ramp: Amellago outcrop transect, High-Atlas, Morocco, pp. 65–88.

Piqué, A., Charroud, M., Laville, E., Aït Brahim, L., Amrhar, M., 2000. The Thethys southern margin in Morocco: Mesozoic and Cenozoic evolution of the Atlas domain, in: Crasquin, S., Barrier, E. (Eds.), Peri-Tethys Memoir 5: New data on peri-Tethyan sedimentary basins. Mémoires du Muséum National d´Histoire Naturelle, Paris, pp. 93–106.

Poisson, A., Hadri, M., Milhi, A., Julien, M., Andrieux, J., 1998. The Central High-Atlas (Morocco). Litho- and chrono-stratigraphic correlations during Jurassic times between Tinjdad and Tounfite. Origin of Subsidence, in: Crasquin, S., Barrier, E. (Eds.), Peri-Tethys Memoir 4: Epicratonic Basins of Peri-Tethyan

Platforms. Mémoires du Muséum National d´Histoire Naturelle, Paris, pp. 237-256.

Quirk, D.G., Pilcher, R.S., 2012. Flip-flop salt tectonics. Geological Society, London, Special Publications 363, 245–264.

Ramberg, H., 1981. Gravity, Deformation and the Earth's Crust, 2nd edition ed. Academic Press, New York.

Rowan, M.G., Jackson, M.P.A., Trudgill, B.D., 1999. Salt-related fault families and fault welds in the northern Gulf of Mexico. AAPG Bulletin 83, 1454–1484.

Rowan, M.G., Lawton, T.F., Giles, K.A., Ratliff, R.A., 2003. Near-salt deformation in La Popa basin, Mexico, and the northern Gulf of Mexico: A general model for passive diapirism. AAPG Bulletin 87, 733–756.

Rowan, M.G., Vendeville, B.C., 2006. Foldbelts with early salt withdrawal and diapirism: Physical model and examples from the northern Gulf of Mexico and the Flinders Ranges, Australia. Marine and Petroleum Geology 23, 871–891.

Saura, E., Ardèvol, L., Teixell, A., Vergés, J., 2016. Rising and falling diapirs, shifting depocenters, and flap overturning in the Cretaceous Sopeira and Sant Gervàs subbasins (Ribagorça Basin, southern Pyrenees). Tectonics 35, 638–662.

Saura, E., Vergés, J., Martín-Martín, J.D., Messager, G., Moragas, M., Razin, P., Grélaud, C., Joussiaume, R., Malaval, M., Homke, S., 2014. Syn-to post-rift diapirism and minibasins of the Central High Atlas (Morocco): the changing face of a mountain belt. Journal of the Geological Society 171, 97–105.

Schaer, J.P., Persoz, F., 1976. Aspects structuraux et petrographiques du Haut-Atlas calcaire de Midelt (Maroc). Bulletin de la Societe Geologique de France Series 7 Vol. XVIII, 1239-1250.

Schultz-Ela, D.D., 2003. Origin of drag folds bordering salt diapirs. AAPG Bulletin 87, 757–780.

Schultz-Ela, D.D., Jackson, M.P.A., 1996. Relation of subsalt structures to suprasalt structures during extension. AAPG Bulletin 80, 1896–1924.

Schultz-Ela, D.D., Jackson, M.P.A., Vendeville, B.C., 1993. Mechanics of active salt diapirism. Tectonophysics 228, 275–312.

Sellier, N.C., Vendeville, B.C., Loncke, L., 2013. Post-Messinian evolution of the Florence Rise area (Western Cyprus Arc) Part II: Experimental modeling. Tectonophysics 591, 143–151.

Souhel, A., Canerot, J., El Bchari, F., Chafiki, D., Gharib, A., El Hariri, K., Bouchouata, A., 2000. The Liassic carbonate platform on the western part of the Central High Atlas (Morocco): stratigraphic and palaeogeographic patterns, in: Crasquin, S., Barrier, E. (Eds.), Peri-Tethys Memoir 5: New data on peri-Tethyan sedimentary basins. Mémoires du Muséum National d´Histoire Naturelle, Paris, pp. 39–56.

Studer, M., Du Dresnay, R., 1980. Deformations synsedimentaires en compression pendant le Lias superieur et le Dogger, au Tizi n'Irhil (Haut Atlas central de Midelt, Maroc). Bulletin de la Societe Geologique de France Series 7 Vol. XXII, 391-397.

Talbot, C.J., 1992. Centrifuged models of Gulf of Mexico profiles. Marine and Petroleum Geology 9, 412-432.

Talbot, C.J., 1995. Molding of salt diapirs by stiff overburden, in: Jackson, M.P.A., Roberts, D.G., Snelson, S. (Eds.), Salt tectonics: a global perspective, AAPG Memoir 65, pp. 61–75.

Teixell, A., Arboleya, M.-L., Julivert, M., 2003. Tectonic shortening and topography in the Central High Atlas (Morocco). Tectonics 22, doi:10.1029/2002TC001460, 002003.

Teixell, A., Barnolas, A., Rosales, I., Arboleya, M.-L., 2017. Structural and facies architecture of a diapir-related carbonate minibasin (lower and middle Jurassic, High Atlas, Morocco). Marine and Petroleum Geology 81, 334–360.

Tesón, E., Teixell, A., 2008. Sequence of thrusting and syntectonic sedimentation in the eastern Sub-Atlas thrust belt (Dadès and Mgoun valleys, Morocco). International Journal of Earth Sciences 97, 103–113.

Vendeville, B.C., 2005. Salt tectonics driven by sediment progradation: Part I - Mechanics and kinematics. AAPG Bulletin 89, 1071–1079.

Vendeville, B.C., Ge, H., Jackson, M.P.A., 1995. Scale models of salt tectonics during basement-involved extension. Petroleum Geoscience 1, 179–183.

Vendeville, B.C., Jackson, M.P.A., 1992. The rise of diapirs during thin-skinned extension. Marine and Petroleum Geology 9, 331–354.

Vendeville, B.C., Jackson, M.P.A., Weijermars, R., 1993. Rates of salt flow in passive diapirs and their source layers, Rates of Geologic Processes, GCSSEPM Fundation 14th Annual Research Conference, pp. 269–276.

Vergés, J., Moragas, M., Martín-Martín, J.D., Saura, E., Razin, P., Grélaud, C., Malaval, M., Joussiaume, R., Messager, G., Sharp, I., Hunt, D.W., 2017. Salt tectonics in the Atlas mountains of Morocco, in: Soto, J.I., Tari, G., Flinch, J. (Eds.), Permo-Triassic Salt Provinces of Europe, North Africa and the Atlantic Margins: Tectonics and hydrocarbon potential Elsevier.

Vially, R., Letouzey, J., Bénard, F., Haddadi, N., Desforges, G., Askri, H., Boudjema, A., 1994. Basin inversion along the North African Margin; The Saharan Atlas

(Algeria), in: Roure, F., Pétrole, I.F.d. (Eds.), Peri-Tethyan platforms, Arles, France, pp. 79–118.

Warsitzka, M., Kley, J., Kukowski, N., 2013. Salt diapirism driven by differential loading — Some insights from analogue modelling. Tectonophysics 591, 83–97.

Weijermars, R., Jackson, M.P.A., Vendeville, B., 1993. Rheological and tectonic modeling of salt provinces Tectonophysics 217, 143–174.

Withjack, M.O., Callaway, S., 2000. Active normal faulting beneath a salt layer: An experimental study of deformation patterns in the cover sequence. AAPG Bulletin 84, 627–651.